Structural and microstructural features of lead-free BNT–BT thin films: Nanoscale electromechanical response analysis

Yanela Mendez-González, Anthony Ferri, Elton Lima, Ahmad Hamieh, Denis Remiens, Aimé Peláiz-barranco, Atair Silva, José Santos Guerra

Structural and microstructural features of lead-free BNT–BT thin films – Nanoscale electromechanical response analysis

Y. Mendez-González,[1,2] A. Ferri,[3] E. C. Lima,[4] A. Hamieh,[5] D. Remiens,[5] A. Peláiz-Barranco,[2] A. C. Silva[1], J. D. S. Guerra,[1,*]

[1]Grupo de Ferroelétricos e Materiais Multifuncionais, Instituto de Física, Universidade Federal de Uberlândia, 38408-100, Uberlândia, MG, Brazil.

[2]Grupo de Materiales Ferroicos, Facultad de Física–Instituto de Ciencia y Tecnología de Materiales, Universidad de La Habana. San Lázaro y L, Vedado. La Habana 10400, Cuba.

[3]Univ. Artois, CNRS, Centrale Lille, Univ. Lille, UMR 8181 – UCCS – Unité de Catalyse et Chimie du Solide, F-62300 Lens, France.

[4]Universidade Federal do Tocantins, 77500-000 Porto Nacional, TO, Brazil.

[5]IEMN-DOAE UMR 8520 CNRS, Université Polytechniques Hauts-de-France (UPHF), Valenciennes, France.

* Author to whom correspondence should be addressed: santos@ufu.br

Abstract

The structural, microstructural and electromechanical properties have been investigated at the nanoscale, as a function of the lanthanum concentration, in $Bi_{0.506}Na_{0.46}Ba_{0.08-3x/2}La_xTiO_3$ (x = 0, 2 and 3 at%) (BNLBT–x) lead-free thin films. The structural characterization, investigated from X-ray diffraction and Raman spectroscopy, confirmed the formation of the perovskite structure and suggest the coexistence of both antiferroelectric (tetragonal) and ferroelectric (rhombohedral) phases. The surface morphology, characterized by atomic force microscopy, has shown a dense and crack-free nanostructured surface for all the studied compositions, noting that the increase in the lanthanum content promoted a decrease of both the grain-size and surface roughness. PFM imaging analyses have evidenced the ferroelectric domain structure over the surface, as well as the presence of non-piezoelectric regions attributed to the antiferroelectric phase. PFM spectroscopy measurements revealed a reliable switching behavior for locally probed ferroelectric domains, yielding a noticeable local piezo-activity, which indeed shows to increase with the increase of the doping content. The static domain-wall was also analyzed in terms of the nanoscale domains structure and the obtained dimensionality indicated a local electric field induced structural disorder. The clear local piezo/ferroelectric nature highlighted on the studied materials underlines the potential for applications of the BNLBT–x films for their integration into advanced electronic nanodevices.

KEYWORDS: lead-free thin films, BNT–BT, piezoelectrics, ferroelectrics, PFM

1. INTRODUCTION

It is known that lead-based ferroelectric compounds, such as $Pb(Zr,Ti)O_3$ and $PbTiO_3$, and others based on them, have attracted most of the attention of the scientific community for several decades due to their excellent piezo-, pyro- and ferro-electric properties.[1–4] However, the lead toxicity and the negative implications to the environment and human health, have conducted to the researchers to re-evaluate their efforts in order to develop environmentally-friendly lead-free materials as an alternative to substitute lead-based systems. An important number of results have been reported in the specialized literature concerning the study and the development of a wide range of lead-free materials, such as: (*i*) perovskite compounds based on $BaTiO_3$ (BT), $Ba_{1-x}Sr_xTiO_3$ (BST), $KNbO_3$ (KN), $LiNbO_3$ (LN), $NaBiO_3$ (NB) and $Ba_{(1-x)}Ca_xTi_{(1-y)}Zr_yO_3$ (BCTZ),[5–9] (*ii*) $A_2B_2O_7$ layered perovskite structures including $Sr_2Nb_2O_7$ (SNO)[10] and $Nd_2Ti_2O_7$ (NTO),[11–12] (*iii*) bismuth layer-structured ferroelectrics based on $SrBi_2Nb_2O_9$ (SBiN)[13] and $Bi_4Ti_3O_{12}$ (BIT),[14] and (*iv*) tungsten bronze oxides such as $Sr_{1-x}Ba_xNb_2O_6$ (SBN) and $Ba_2NaNb_5O_{15}$ (BNN),[15,16] or more recently those containing A_2MO_6-type compounds such as La_2WO_6 (LWO)[17] and Nd_2WO_6 (NdWO).[18]

Among this non-exhaustive amount of lead-free compounds, the potassium sodium niobate $(K_{0.5}Na_{0.5})NbO_3$ (KNN), the bismuth potassium titanate $(Bi_{0.5}K_{0.5})TiO_3$ (BKT) and the bismuth sodium titanate $(Bi_{0.5}Na_{0.5})TiO_3$ (BNT) based systems, are examples of materials showing remarkable piezoelectric properties.[19–21] In particular, the $(1-x)Bi_{0.5}Na_{0.5}TiO_3–xBaTiO_3$ (BNT–BT) compound has been considered as one of the promising lead-free piezoelectric materials.[22–24] For this system, similarly to the $Pb(Zr,Ti)O_3$, it has been stated a morphotropic phase boundary (MPB) delimiting the presence of the rhombohedral (R3*c*) and tetragonal (P4*mm*) phases, where the dielectric and piezoelectric properties are enhanced.[22,25] It has also been reported that the MPB holds an antiferroelectric (P4*bm*) phase, separating the tetragonal (P4*mm*, BT-rich) and rhombohedral (R3*c*, BNT-rich) ferroelectric phases.[23]

From the technological point of view, the need for the integration of lead-free piezoelectric materials in microelectronic devices makes the fabrication of thin-films a priority assignment for the construction of non-volatile memory devices, as well as for high-speed and low-power electronic applications.[26] The high compositional control required to obtain films with composition close to the MPB in these complex oxides makes chemical solution deposition (CSD) processes one of the most appropriate techniques to fabricate $BNT_{(1-x)}$–BT_x thin-films.[27,28] Other advantages of this method include the low cost, effective to fabricate high-quality ferroelectric films with good stoichiometry control as well as a chemical homogeneity and uniform film over a large area.[27] In this context, several investigations have been conducted on BNT_{1-x}–BT_x thin-films particularly for those compositions close to the MPB.[29–33] For instance, structural properties studied on (1-*x*)$Bi_{0.5}Na_{0.5}TiO_3$–*x*$BaTiO_3$ films (with x = 0, 0.1, 0.9 and 1.0) revealed a rhombohedral symmetry for the pure BNT and BNT–0.1BT compositions, as well as a tetragonal symmetry for the BNT–0.9BT compositions.[29,30]

On the other hand, Cernea *et al.* reported studies for the $0.89(Na_{0.5}Bi_{0.5})TiO_3$–$0.11BaTiO_3$, ($BNT–BT_{0.11}$)[30] as well as $(Bi_{0.5}Na_{0.5})_{0.95}Ba_{0.05}TiO_3$ ($BNT–NT_{0.05}$)[31] thin films, both fabricated via a sol-gel process and spin-coating technique. These researches revealed the formation of the cubic structure for the $BNT–BT_{0.11}$ thin film,[30] as well as the crystallization of the rhombohedral structure for $BNT–BT_{0.05}$ composition.[31] Moreover, other structural properties have also been previously investigated for the (1-*x*)$Bi_{0.5}Na_{0.5}TiO_3$–*x*$Bi_{0.5}K_{0.5}TiO_3$ [BNT–BKT–100*x*] thin films,[34,35] where the presence of the perovskite phase without specifying the symmetry-type has been reported. However, despite the extensive reports on the physical properties related to the BNT–BT system, most of them carried out in ceramics, no clear understanding of the phase diagram has been offered to date.

Recently, special attention was paid to the $(Bi_{0.50}Na_{0.50})_{0.92}Ba_{0.08–3x/2}La_xTiO_3$ ceramic system.[36,37] Indeed, detailed research regarding the structural, ferroelectric and dielectric

behavior has then been reported by Mendez-Gonzáles *et al*.[36,37] For such ceramics, the structural analysis has revealed the coexistence of both ferroelectric (P4*mm*) and antiferroelectric (P4*bm*) tetragonal phases for the lanthanum-free composition. However, for the lanthanum modified compositions, both antiferroelectric tetragonal (P4*bm*) and ferroelectric rhombohedral (R3*c*) phases have been shown that coexist. On the other hand, the Polarization – Electric field (P–E) hysteresis loops have suggested a higher stability of the ferroelectric phase for x = 0, 2 and 3 at% La at room temperature. The antiferroelectric phase has been shown to be more stable at room temperature for x = 1 at%.[36] Interesting results have also been shown concerning the electrocaloric effect on these ceramic materials.[38,39]

Nevertheless, to the best of our knowledge, there are no previous systematic studies carried out in the (Bi,Na,La)(Ba,Ti)O_3 system when grown in thin films. In addition, nanoscale physical properties of the matter required to be probed since they can govern the global performance of the devices at the macroscopic scale. For this, atomic force microscopy (AFM) technique is known as a powerful non-destructive tool for high-resolution characterization of matter on the nanoscale. In particular, the piezoresponse mode (PFM) of the AFM offers the opportunity for imaging and characterizing ferroelectric thin films by assessing domain structure, switching behavior and electromechanical activity.[40,41] In this framework, the PFM seems to be very suitable for probing local electrical properties of such (Bi,Na,La)(Ba,Ti)O_3 thin films.

The present work aims the investigation of the structural, microstructural and local electrical properties of $Bi_{0.506}Na_{0.46}Ba_{0.08-3x/2}La_xTiO_3$ (x = 0, 2 and 3 at%) lead-free thin films. In particular, a comprehensive study on the structural characteristics, which indeed have not been previously reported, is presented. The room temperature piezoelectric and ferroelectric performances of the films were particularly investigated on the nanoscale by using imaging and spectroscopic PFM approaches. Specific emphasis is devoted on the opportunities of these thin films for further development of advanced electronic devices.

2. EXPERIMENTAL PROCEDURE

$Bi_{0.506}Na_{0.46}Ba_{0.08-3x/2}La_xTiO_3$ lead-free thin films, considering x = 0, 2 and 3 at %, were synthesized via a sol-gel process by the spin-coating technique. Bismuth (III) acetate ($(CH_3COO)_3Bi$, > 99.99 %, Aldrich), sodium acetate (CH_3COONa, > 98 %, Synth) and barium acetate ($(CH_3COO)_2Ba$, > 99 %, Synth) were separately dissolved in acetic acid (99 %, Synth) producing transparent stock solutions. Then, titanium (IV) isopropoxide, 97 % solution in 2-propanol ($Ti\{OCH(CH_3)_2\}_4$, Aldrich), was added drop by drop under magnetic stirring at 80 °C for 240 min. A chemical stabilizer was included during solutions synthesis in order to increase the stability of titanium isopropoxide. After this process, yellowish colored stable gels were obtained. *N, N*-dimethylformamide (99.8 %, Neon) was used to minimize the formation of cracks during the drying and the annealing steps. The precursor-solutions were obtained considering 10 mol % excess bismuth, in order to compensate its high volatility, and deposited on $Pt(111)/TiO_2/SiO_2/Si$ substrates with a spinning speed of 7000 rpm for 40 sec. The films were preheated at 150 ^oC for 30 min in order to evaporate the solvent, and then the pyrolysis process was carried out at 450 ^oC for 30 min in order to remove other organic compounds. This step was repeated until the desired thickness was obtained. The coated films were finally annealed at 700 ^oC for 60 min to complete crystallization. The samples were hereafter labeled as BNLBT–*x*, where BNLBT–0, BNLBT–2 and BNLBT–3 correspond to x = 0, 2 and 3 at% La, respectively.

The phase compositions of the near-surface layers were examined at room temperature by grazing incidence X-ray diffraction analysis (GIXRD) using an XRD6000 (Shimadzu) diffractometer with Cu-K_α (0.15406 nm) radiation. In order to study the structure of the films in depth profile, X-ray diffraction (XRD) measurements were collected at a fixed angle of 8° and a scanning angle from 20° to 80°. This GIXRD method has been carried out in order to reduce the contribution of the substrate (Pt) to the XRD pattern. Structural refinement was

performed through the Rietveld method, using the GSAS software suite and EXPGUI interface.[42,43] The unit-cell parameters, atomic positions, scale factor, background and line-shape parameters were refined during the fitting processes. The peak profiles were fitted using the Thompson-Cox-Hastings pseudoVoigt function,[44] while a sixth-order polynomial was used to fit the background. Raman data were collected, at room temperature, by using a micro-Raman Horiba Jobin Yvon (LabRam HR Evolution) spectrometer with a 532 nm laser. Local electromechanical experiments were performed using AFM (MFP-3D, Asylum Research/Oxford Instruments) under ambient conditions. The surface morphology and roughness were characterized in Tapping mode. Piezoelectric and ferroelectric behaviors were investigated with the PFM tool using Pt/Ir coated probes (PPP-EFM, NanoSensors) and stiff cantilevers (k ~3.8 N/m). Dual AC resonance tracking (DART)[45] mode was employed for PFM analysis in order to enhance the piezoelectric signal, under a driving voltage V_{AC} of 2 V at the probe tip and by grounding the conductive substrate. PFM in spectroscopic mode was used to evaluate piezoelectric deformation and switching behavior of the domains located beneath the AFM tip by recording piezoresponse loops.

3. RESULTS AND DISCUSSION

3.1 Structural analyses

Figure 1 shows the room temperature XRD patterns for the as-prepared BNLBT–x thin films. For the sake of comparison, the XRD patterns of the standard BNT system, with tetragonal (P4bm)[46] and rhombohedral (R3c)[47] symmetries, and the platinum (Pt) from the electrode contribution, with cubic (Fm-3m) symmetry,[48] are also shown in the Figure 1. A minor $Bi_2Ti_2O_7$ pyrochlore secondary phase is marked with an asterisk. The crystalline structures of the BNLBT–x films analyzed based on their XRD patterns correspond well with the BNT-based perovskite structure, with a well-developed crystallinity, for all the studied compositions.

Results indicate that the above-mentioned synthesis method is effective in preparing perovskite BNLBT–*x* thin-film structures with a wide range of composition *x*. The crystal structures of the films are also found to be in agreement with the reported results by Zheng *et al.*[29] and are similar to those previously reported for BNLBT–*x* ceramics.[36] For complementary information, cross-sectional SEM images, collected by using a JEOL JSM-840 Microscope (Germany), have been obtained in order to estimate the thickness of the studied films. The inset of Figure 1 displays the result for the BNLBT–2 film as a representative, with no apparent difference for the other compositions, indicating to be dealing with films showing a thickness of about 400 nm.

Figure 1.

Recent studies have reported a coexistence between two tetragonal phases (P4*bm* and P4*mm* space groups) for BNT–BT ceramics, where the (111) and (200) pseudocubic reflections, observed for 2θ values around 40.0° and 46.5°, respectively, appear as singlet and doublet, respectively.[36] Considering lanthanum-modified compositions, however, it was assumed the coexistence between the rhombohedral ferroelectric (R3*c* space group) and tetragonal antiferroelectric (P4*bm* space group) phases, as the lanthanum content increases. As a result, different to the pure system, a splitting in the (111) reflection is observed, together with the splitting in the (200) reflections, thus revealing the doublet character for both pseudocubic reflections. Nevertheless, different to the results reported for ceramics, the X-ray diffraction patterns for the thin films studied in the present work have shown relative broader profile peaks, with not very well resolved reflections, the result of which can be attributed to the overlapping of different diffraction reflections as well as the intrinsic microstructural properties such as small grain-size distribution and additional stresses driven by the interface effects, typical in thin films.[49,50] The existence of an induced strain (or mechanical tensile) at the film-substrate

interface, caused by the different thermal expansion coefficients between the film and the substrate, significantly reflect in the physical properties of the thin films.

In this context, a detailed investigation on the structural characteristics of these thin films was carried out by a refinement analysis of the above XRD patterns, the results of which are shown in Figures 2(a)–(c). The experimental (observed) and theoretical (calculated profiles) data are represented by symbols and solid lines (in red), respectively. The vertical marks, below the patterns, correspond to the calculated Bragg's reflections. The differences between the experimental and theoretical data are identified by bottom blue lines. Four different initial structural models were considered for the calculation of the diffraction patterns: (*i*) tetragonal (T), with P4*bm* space group (ICSD-280381),[46] (*ii*) rhombohedral (R), with R3*c* space group (ICSD-280983),[47] (*iii*) cubic phase (C_1), with F*m*-3*m* space group (ICSD-64923),[48] in order to reproduce the contribution of the substrate (Pt) and (*iv*) cubic-phase pyrochlore (C_2), with F*d*-3*m* space group (ICSD-99437), for the simulation of the secondary phase percentage.[51] The starting structural data for refinement were taken from the "Inorganic Crystal Structure Database" (ICSD).[52] It is worth noting that, while most of the reflections demonstrate the same relative peak intensities for all the lanthanum concentrations, a noticeable increase in the intensity can be observed for the $(111)_{C1}$ plane around $2\theta \approx 39.83°$ as the lanthanum content increases. Although the used GIXRD method reduces the contribution of the substrate to the XRD pattern, it is important to point out that the penetration depth profile inside the film strongly depends on the incidence angle and the attenuation coefficient of the material.[53] In fact, the increase in the intensity of the $(111)_{C1}$ reflection is a clear indicative for the increase of the substrate contribution. In addition, it can be observed a change in the DRX profile for the patterns around 46.5°, as can be confirmed in the insets of Figures 2(a)–(c). The refined profiles for this region suggest a tendency of splitting for the BNLBT–0 composition, with a trend for the formation of a single reflection with the increase of the lanthanum concentration, as

observed for the BNLBT–3 thin film. This tendency provides an important qualitative information about the structure of the BNLBT–*x* films and indirectly infer about the phases' coexistence with the increase of the La content. Similar results have been reported in the literature for La-doped BNT–BT ceramics with the same compositions, showing the coexistence of both tetragonal (P4*bm*) and rhombohedral (R3*c*) phases by transmission electron microscopy (TEM).[54]

Figure 2.

Table 1 illustrates the unit-cell (*a*, *b* and *c*), volume (*V*) and goodness-of-fit (R_{wp}, R_p and χ^2) parameters, as well as the phases fractional weight (*w*), calculated from the refinement process. The final atomic parameters of the lattice sites (*x*, *y*, *z*) were also calculated from the simulation with a very low standard deviation for the four involved phases, the result of which are not shown in Table 1 because of the large amount of data. The obtained values for R_{wp}, R_p and χ^2 are indicative of a high-quality data refinement, evidencing a good agreement between the experimental (observed) and theoretical (calculated) results.[43]

Table 1.

For a better analysis of the structural properties from refinement results, the behaviors of the lattice parameters (*a* and *c*) for both tetragonal (T) and rhombohedral (R) phases, as well as the phases fractional weight reported in Table 1, as a function of the La content (*x*), are shown in Figures 3(a) and 3(b), respectively. The calculated lattice parameters reveal no significant variation with the increase of the lanthanum concentration, the values of which fall in the range of those reported in the literature for bulk materials.[36] This result could be due to the

considerable achieved films thickness (around 400 nm). As observed from Figure 3(b), different to the obtained results for their ceramic counterparts, the refinements for the thin films confirmed the coexistence of the tetragonal antiferroelectric (AFE) and rhombohedral ferroelectric (FE) phases for the studied BNLBT–*x* films, revealing the major contribution of the AFE phase for the BNLBT–0 and BNLBT–2 compositions. The phases fraction also revealed an increase in the C_1 phase, from 2.5 % up to 15.1 %, with the increase of the lanthanum content from 0 to 3 %, respectively. This result, which can be better observed in Figure 3(c), confirms the increase of the substrate contribution, as previously suggested from the analysis of the intensity for the $(111)_{C1}$ reflection around 39.83°. It can be seen, however, that the fractional weight of the tetragonal AFE phase decreases, whereas the contribution of the rhombohedral FE one increases, with the increase of the lanthanum concentration. In this way, it is worth noting that for the BNLBT–3 composition, an inversion in the phases fraction has been observed, showing the major contribution for the FE phase (44.5 %), while the fractional weight for the AFE, cubic-C_1 (Pt) and cubic-C_2 (pyrochlore) phases were found to be around 39.4 %, 15.1 % and 1.0 %, respectively. Furthermore, as can be seen, a very low fractional weight (< 3 %) for the C_2 pyrochlore phase ($Bi_2Ti_2O_7$) was also confirmed for all the compositions. Thus, the splitting observed in the inset of Figure 2(a) for the reflection around 46.5°, which revealed to be more evident for the BNLBT–0 and BNLBT–2 compositions, clearly agrees with the refinement results (phase fractional weight), showing the major contribution of the AFE phase (with tetragonal symmetry) for these compositions.

Figure 3.

Raman spectroscopy was also used to analyze the structural properties and phase evolution of the studied BNLBT–*x* thin films. The Raman data are shown in Figure 4 for the studied

compositions, in which the spectral signature for BNT-type perovskites is confirmed, represented by three typical regions identified as I, II and III in the Raman spectra.[55–57]

Figure 4.

In order to better explore the Raman results, the experimental data have been fitted by considering a theoretical mathematical model based on the location of the curvature maxima in concave-down (CMCD) spectral regions, reported by Buixaderas *et al.*[58]. Results are shown in Figure 5, where Raman scattering spectra (open symbols) as well as the fitting results (solid-lines) and the decomposed active modes into individual Lorentzian components (dashed-lines) have been included for the studied compositions.

Figure 5.

The peak's position for each Raman active mode (natural wavenumber, cm^{-1}), obtained at room temperature after the fitting procedure, as well as their symmetry modes are presented in Table 2 for the compositions. Results reveal that seven active modes are located for the BNLBT–0 sample, whereas eight modes were observed for the BNLBT–2 and BNLBT–3 compositions in the whole analyzed wavenumber range. The additional modes detected for the modified samples, and observed below 200 cm^{-1}, could be related to the overlapping of the modes associated with the La–O vibration in this spectral region. In addition, a noticeable dependence of the wavenumber for several vibrational modes on the lanthanum concentration can be observed, which have been identified as M_2, M_4, M_5 and M_6 in Table 2.

Table 2.

The vibrational modes for both tetragonal and rhombohedral contributions have been identified (scripted by T and R, respectively, in both Figure 4 and Table 2) and the peaks were indexed accordingly. In the region I, below 200 cm^{-1}, the vibrational modes are associated with the A–O stretching vibrations,[55] involving in that case the Bi, Na, Ba cations for the BNLBT–0 sample and also La cations for the BNLBT–2 and BNLBT–3 compositions. The Raman bands between 200 and 400 cm^{-1} (region II) are related to the Ti–O stretching vibrations,[56] and the stretching modes related to the TiO_6 oxygen octahedral are assigned to the higher wavenumbers of the spectra (region III, above 400 cm^{-1}).[57] Previous report, regarding bulk ceramic BNLBT–*x* compositions, revealed the coexistence of tetragonal and rhombohedral phases.[37] For the undoped sample (*x* = 0), the vibration modes have been associated with both P4*mm* and P4*bm* tetragonal phases, while for lanthanum-doping bulk ceramics the Raman spectra have shown the coexistence of both R3*c* rhombohedral and P4*bm* tetragonal phases. As observed, the obtained results on the structural properties from XRD and Raman spectroscopy are in agreement with the results reported for their bulk ceramics counterparts, which could confirm a possible phase coexistence for the studied thin films. However, in order to better clarify this issue, additional quantitative analyses are needed, which include the temperature dependence of both Raman spectroscopy (considering not only the behavior of the peak positions, but also for the full-width at half-maximum and intensity of the Raman modes) and higher resolution XRD measurements, as a function of the lanthanum concentration. Such investigations are in progress and the results will be presented in further works.

3.2 Nanoscale microstructural features and electromechanical response

Nanoscale surface and electromechanical properties were then probed. The characteristic AFM surface topography is shown in Figure 6 for the different compositions: (i) BNLBT–0, (ii) BNLBT–2 and (iii) BNLBT–3. The images have been recorded over the 5×5 μm^2 and 2×2 μm^2 scan regions (a and b, respectively); the grain-size distributions are also shown in Figure

6(c). Regardless the La content, it is observed a dense and crack-free nanostructured surface. However, by looking in more detail, it can be noticed some differences. In the case of the pure BNLBT–0 film (i), as depicted in Figures 6(a)–(c), irregular large grains are observed whose lateral size is ranging from 200 nm up to 900 nm, exhibiting a Gaussian grain-size distribution with an average grain size around 230 nm. For the BNLBT–2 sample (ii), while an onset of coalescence seems to be observed, nanosized rounded grains with diameter ranging between 50 and 130 nm are obtained, resulting in an average grain size around 92 nm. On the other hand, it can be observed that the BNLBT–3 composition (iii) presents randomly-oriented elongated grains with typical widths of about 30 nm and lengths ranging from 50 to 250 nm, with an average grain size around 87 nm. The root mean square roughness, measured over a 10×10 μm^2 scan area, was found to be around 20.0, 10.6 and 10.4 nm for the BNLBT–0, BNLBT–2 and BNLBT–3 films, respectively. It can be observed, therefore, from these AFM measurements that the introduction of the lanthanum cations promoted a decrease of both the grain size and the surface roughness, allowing for the integration of such films into nano-devices to be considered.

Figure 6.

The observed lanthanum concentration dependence of the average grain-size could be associated with an increase of the structural defects (i.e. charged point defects, vacancies, defect-dipole and/or ionic charges) as the doping content increases. Previous evidences, reported for $BaTiO_3$-based ceramics,[59] indicate that the grain growth inhibition is associated with the creation of vacancies, which lead to the space-charge accumulation into the grain boundaries, hence causing a decrease in the grain size. For the studied BNLBT–*x* thin films, positive vacancies are created due to the substitution of the Na^+ and/or Ba^{2+} ions by the rare-

earth cation (with 3+ valence) at the dodecahedral sites of the perovskite structure. It is worth noting that the charge compensation requires that the positive charges excess, resulting from the donor-doping ion, takes place by sodium vacancies (V'_{Na}), barium vacancies (V''_{Ba}) and/or titanium vacancies (V''''_{Ti}). Therefore, the La doping ion could act as a grain growth inhibitor thus promoting a domain-wall pinning effect on the grain boundary with the increase of the lanthanum content. In this context, an increase of the V'_{Na}, V''_{Ba} and/or V''''_{Ti} defects concentration with the increase of the lanthanum content is believed to be a possible cause for the decrease of the average grain-size in the studied thin films. It is worth noting, however, that additional analyses regarding the effect of such positive vacancies, as well as the possible influence of oxygen vacancy defects, will be better explored throughout the investigation of the macroscopic properties (temperature dependence of the dielectric response and macroscopic polarization), and will be in fact the focus of a further work.

Electroactive performances of the films were investigated by measuring the piezoelectric and ferroelectric properties on the nanoscale by PFM measurements. Figure 7 depicts the as-grown out-of-plane (OP) amplitudes (a, c and e) and phase PFM patterns (b, d and f) detected over the surfaces for the BNLBT–0 (a, b), BNLBT–2 (c, d) and BNLBT–3 (e, f) compositions. High electromechanical activity has been detected for all the films as evidenced by the strong contrasts observed on the amplitude PFM images and related to the local deformation of the layer under the AFM tip. This result confirms the enhanced piezo-activity for the studied thin films. Comparing the contrasts of the three samples, higher electromechanical activity is detected for the doped BNLBT films, as seen on the corresponding dark blue-to-yellow contrast scales under similar driving voltage. Phase PFM images (b, d and f) simultaneously recorded also exhibit contrasts associated to the ferroelectric response of the films due to the OP components of the polarization vector in the layer. The various contrasted regions reveal upward and downward polarized ferroelectric domains randomly distributed in the layers,

showing a clear domain structure. Besides, both PFM signals are strongly dominated by the surface morphological features. Furthermore, regions with very low deformations are observed on the amplitude PFM images, as highlighted by the white circles on the Figures 7(a), (c) and (e). These zones with very limited piezo-activity could be attributed to antiferroelectric phases existing in the fabricated films, which corroborate the aforementioned phase coexistence suggested through the structural characterizations, containing both the tetragonal antiferroelectric (P4*bm*) and rhombohedral ferroelectric (R3*c*) phases.

Figure 7.

To get better insight into switching and electromechanical behavior of the samples, phase and amplitude PFM loops were simultaneously recorded over the free surface of the films in remnant mode (at zero DC bias field), in order to minimize electrostatic contribution. The AC driving voltage was intentionally reduced to be much smaller than the coercive voltage of the films, thus avoiding additional interference with switching instabilities. Figure 8 shows remnant phase (a, c and e) and amplitude PFM loops (b, d and f) for the BNLBT–0 (a, b), BNLBT–2 (c, d) and BNLBT–3 (e, f) compositions. The obtained piezo-loops are representative of the average response from the active layer, based on the statistical study of 30 measurements performed over the surface, the result of which revealed very similar piezo-responses thus indicating homogeneous surfaces for all the studied compositions and confirming the quality of the thin films. The phase signals lead to the occurrence of a typical hysteresis loop with two stable polarization states associated with the switching properties of the probed domain beneath the AFM tip, confirming the good ferroelectric response of the films. The coercive voltage values (V_C), determined from the piezo-loops, are found to be much lower for the pure BNLBT–0 sample (V_C ~ 13 V), suggesting a more reliable switching capability, as compared to the

lanthanum modified compositions (V_C ~ 20 V). A similar trend in the switching efficiency with the increase of the lanthanum content has been observed for La-modified BNT–BT ceramic bulk compositions,[36] obtained from the solid-state conventional sintering method, where the coercive field (E_C) was determined from macroscopic polarization *versus* electric field (P–E) measurements. The obtained result could be ascribed to the AFE and FE crystalline phases mixing, with the particular feature to be leading here with the major contribution of the AFE component for the pure BNLBT–0 thin film composition. This is particularly true on the nanoscale, where the energy required to efficiently switch the polarization of the probed domain beneath the AFM tip is highly dependent on the crystallite orientation.[60–62] As a consequence, the lower coercivity for the polarizing voltage obtained on the BNLBT–0 film is in good agreement with the minor contribution of the ferroelectric rhombohedral crystallites, compared to the case of the La-doped films where the FE component becomes the dominating phase, as indeed previously confirmed by the structural analyses.

In the case of the amplitude PFM signals, as shown in Figures 8(b), (d) and (f) for the BNLBT–0, BNLBT–2 and BNLBT–3, respectively, well-defined butterfly-like shapes are observed, which confirm the electromechanical behavior related to the converse piezoelectric effect. By considering the PFM loops recorded over the BNLBT–0 surface, for instance, it can be noted a saturation in the local mechanical response at maximum bias voltage leading to an amplitude deformation *A* of ~5.45 nm. Since this signal is enhanced by the use of the contact resonance through the DART PFM method, this implies taking into account the quality factor *Q*, which is around 80 for such inorganic compound where the loss is too low.[18,63] Therefore, by considering the detected PFM amplitude proportional to $A = d_{33}V_{AC}Q$ it can be estimated the effective piezoelectric constant value to be around d_{33eff} ~ 34 pm/V. This result is in good agreement with the reported value for BNT thin films ($d_{33eff.max}$ ~ 47 pm/V) with similar thickness and deposited on silicon substrates by the sol-gel method.[64] The PFM amplitude

signal also depicts an increase in the *A* values for the BNLBT–2 and BNLBT–3 compositions, at the same maximum applied DC voltage. Therefore, higher d_{33eff} values are expected for the La-doped samples, since they have not reached their saturated loops condition, thus suggesting an enhanced local piezo-activity with the increase of the lanthanum content. This result also confirms the obtained results from the XRD properties, and reveals the potential of the lead-free BNLBT thin films to replace compounds containing toxic elements such as lead-based materials. Furthermore, each measured amplitude loop exhibits a symmetric shape when considering the maximum deformation under both positive and negative voltages excitation. This behavior reveals the homogeneous electromechanical properties of the studied films, thus enabling their use in actuators, sensors or energy harvesting devices.

Figure 8.

It is worthwhile noting that during switching PFM spectroscopy, in some cases no signal was detected. This particular behavior could be related to the absence of piezo-activity shown on the amplitude PFM images in Figures 7(a), (c) and (e) for the BNLBT–0, BNLBT–2 and BNLBT–3 compositions, respectively, attesting that antiferroelectric regions could have been probed by the AFM tip. To the best knowledge of the present authors, only three studies have been reported on the recording of piezo-response loops on antiferroelectric materials, where an incipient double hysteresis loop has been shown.[65–67] Therefore, from the obtained PFM analyses, the observed domain pattern, combined with the local switching behavior and electromechanical activity, is a clear evidence of the nanoscale piezo-/ferroelectric nature at room temperature for the studied BNLBT–*x* thin films. Besides, it is worth noting that the probing of AFE-FE phase transition by PFM has just been recently reported in $PbZrO_3$ capacitors.[68] As a remark, it is worth pointing out that the hysteresis loops are systematically

shifted along the DC bias axis, towards positive voltages. This asymmetry is characteristic of an imprint behavior of the local switching, which commonly arises from the presence of a built-in electric field in the samples.[69,70] In order to better evaluate the imprint effect, the voltage offset (V_{off}) of the hysteresis loops has been obtained by averaging the negative and positive coercive voltages (V_C^- and V_C^+, respectively) through the following relation: $V_{\text{off}} = (V_C^+ + V_C^-)/2$.[71,72] Results reveal a decrease in the voltage offset value, from about 7 V for the pure sample up to around 5 V for the La-doped compositions, showing a strong influence of the doping cation in the imprint effect.

From the fundamental point of view, although the real nature of this imprint behavior observed in thin films still remains under intense discussions by the scientific community, thus remaining as a non-fully clarified issue up today, several phenomenological models have been proposed to explain the origin of the observed phenomenon.[72–76] In fact, there has been a consensus that an internal electric field developed by charged defects is believed to play an important role in the imprint phenomena. In this way, two of the most accepted models in the current literature with a better description of the imprint effect are probably those related to the defect-dipole alignment, proposed firstly by Arlt *et al.*[74] and later modified by Warren *et al.*, [76] and the interface screening process, proposed by Grossman *et al.*[72] According to the defect-dipole alignment model, the asymmetric distribution of trapped charges and the alignment of defect-dipoles near the material-electrode interface have been suggested to be responsible for the voltage shift in ferroelectric thin films.[76] The defect-dipole alignment produces an internal bias electric field, which induces a voltage shifts thus promoting the imprint effect. On the other hand, the interface screening model considers the presence of a very thin layer at the film-electrode interface where there is a suppression in the spontaneous polarization.[72] This model, which in fact shows to be a modification of the defect dipole alignment model, considers the redistribution of electrons and/or holes as the main cause for the imprint phenomena observed

in ferroelectric thin films, being the defect-dipole alignment, a secondary imprint mechanism. The origin of the voltage offset has been related, in this case, to a large internal electric field originated within the interface layer of the film, with the orientation along the polarization direction. A gradual shifting of the hysteresis loop is thought to be governed, therefore, by the internal field due to the consecutive electronic charges trapping, which are injected from the electrode into the film and have a polarity in the opposite direction to the ferroelectric dipole. As a consequence, the induced internal field screens the applied external electric field and a higher applied voltage is required to induce the polarization reversal.

As observed from the proposed models, whatever the mechanism that promotes the voltage offset, there have been several strong indications that the defects play the essential role in the polarization degradation phenomena, which result in the asymmetric switching 'imprint' behavior. The main idea of the defect chemistry models is that the charge electroneutrality could be distorted by the inclusion of doping cations,[72,74] which possess a different valence than the hosting ions they replace. Therefore, the observed imprint behaviors in this work could be explained considering to the role of the defects, and described according to the following scenario:

It is well known that in ferroelectric perovskites (ABO_3) intrinsic defects related with evaporation of some alkali cations, and some other di- and tri-valent elements, during processing and sintering at high temperatures are often present in the material. In order to compensate the charges unbalance promoted by cations volatilization, thus maintaining the charge neutrality, oxygen vacancies are commonly created, which significantly affect the physical properties of the studied system.[77] Therefore, oxygen vacancies, which have indeed revealed as the most mobile ionic defects in perovskites, and natural intrinsic oxygen-vacancy-related defect dipoles, have been shown to be involved in most of the observed anomalous behaviors in the electrical and electromechanical properties of ferroelectrics and related

materials.[78] Such defects have been suggested, for instance, to play a crucial role in the intrinsic polarization mechanisms and the domain-wall dynamics, thus promoting the voltage offset that leads to the imprint effect.[79] However, the formation and mobility of defects can be easily controlled by the partial substitution of A- (or B-site) cations, with acceptor and donor species, thus reducing the defect density and improving most of the physical properties. In BNT-based systems, for instance, the evaporation of Na, K and Bi may result in many nonstoichiometric structural defects to form secondary phases during the thermal processes.[80] As a consequence, a noticeable imprint behavior could be expected, as indeed observed for the pure BNLBT–0 sample. Nevertheless, taking into account that donor doping does mainly introduce immobile defect dipoles, the inclusion of the La^{3+} cation, which suppresses the formation of oxygen vacancies, could have led to a decrease of the mobile defect dipole concentration and, therefore, to a reduction of imprint, as observed for the La-doped concentrations (BNLBT–2 and BNLBT–3). This result is in agreement with those reported in the literature for some perovskite-based structure ferroelectric systems.[72,74]

3.3 Domain structure nature and fractal dimension analysis

In order to investigate the domain structure in more details, as well as to obtain a quantitative description of the polarization distribution, additional analysis involving the autocorrelation function has been carried out from the PFM results previously discussed (Figure 7). The PFM data have been processed using the Gwyddion image analysis program.[81] To illustrate the domain structure nature of the thin films produced in this work, the autocorrelation function $C(r)$ was applied to quantify the nanodomain structure in terms of the average correlation length (Δ). In this way, important information can be extracted from the OP images obtained for the studied BNLBT–*x* thin films, by applying the transformation on the piezo-response images in Figures 7(a), (c) and (e) following the theoretical model recently reported

by Shvartsman *et al.*[82] According to this model, the short-range correlation length can be obtained from the autocorrelation function, by Equation (1), where *r* is the distance from the central maximum and *b* is the exponential parameter $(0 < b < 1)$.

$$C(r) \propto \exp\left[-\left(\frac{r}{\Delta}\right)^{2b}\right] \quad (1)$$

Taking into account the autocorrelation images (not shown here), the autocorrelation function *C*(*r*), at small *r* values, were recorded for all the studied BNLBT–*x* compositions. Figure 9(a) depicts the distance (*r*) dependence of autocorrelation function *C*(*r*) over all in-plane directions for the BNLBT–0 composition, as an example of the obtained results for all the studied compositions, where the values have been normalized to *C*(*r=0*). The average correlation length value obtained from the best fitting of the curve for the BNLBT–0 thin film was found to be around 66.2 ± 0.2 nm.

Figure 9.

The average correlation length (Δ), the fractal dimension of the "polarization interface", and roughness exponent (ξ) for the BNLBT–*x* thin films as a function of the La content (*x*) are shown in Figure 9(b). The correlation length obtained from the fitting process by using the autocorrelation function, Equation (1), increases from 66 nm up to 529 nm with the increase of the lanthanum contents from 0 % to 3 %. The lower correlation length value, which has been indeed obtained for the BNLBT–0 film, revealed to be close to that reported for classical relaxor systems, such as PMN single crystals ($\Delta \approx 70$ nm),[82] suggesting the possible relaxor character for the studied film. It has been also reported that, for PMN–*x*PT single crystals, such Δ value reveals to be strongly dependent on the PT content, reaching the higher value (~ 650 nm) for

the highest titanium content composition.[82] For other relaxor systems, such as PLZT thin films, intermediate Δ values (close to 350 nm) have also been reported,[83] suggesting a strong relationship between the grain size and correlation length. For BNT–BT materials, instead, a lower value for the correlation length have also been recently reported in single crystals, revealing to be around 20 nm.[84] However, different to those previously discussed here, the correlation length obtained for that single crystal composition has been extracted from diffuse X-ray scattering experiments. Results obtained in this work, from Figure 9(b), show that the characteristic length scale of switched domains obtained for the BNLBT–3 thin film (529 nm) is significantly higher than the average grain size (87 nm) for the same composition, which is a clear indicative of the presence of long-range correlations. In fact, the correlation length has been related to the size of the polar nano regions (PNRs) in relaxors materials.[85] Therefore, the high correlation length values obtained in the present work suggest the higher size of the PNRs for the BNLBT–3 composition. The observed trend for the correlation length also reveals to be in agreement with the results obtained from the structural properties, showing an increase in the FE phase contribution with the increase of the lanthanum content.

According to the Kolmogorov-Avrami-Ishibashi (KAI) model, domain switching processes can be associated to fractal dimensionality.[86] From the fundamental point of view, several theoretical models have been proposed and used in the literature, to account for the microstructural characteristics of electronic materials based on fractal analyses.[87,88] In this context, intergranular phenomena at the nanoscale dimension could be investigated by considering their fractal nature.[88] Such analyses significantly contribute for researches devoted to microelectronic miniaturization and undoubtedly provide new perspectives for the application of ferroelectric and related materials in electro-electronic devices with very high integration technology.[89] Therefore, in order to better understand the mechanisms responsible for nucleation of nanodomains as well as the change in domain-wall geometry under the action

of an external electric field, a fractal analysis has also been performed. The fractal dimension from the OP–PFM images were calculated by using the cube counting method with the abovementioned image data analysis. In the cube counting method, a cubic lattice with lattice constant C is superimposed on the z-expanded surface. The slope of the linear portion of a log(area) vs log(C) plot provides the fractal dimensionality (D).[90] Based on these linear fittings (not shown here), the dimensionalities were found and summarized in Figure 9(b) for all the studied BNLBT–*x* compositions. Notice that for the BNLBT–0 and BNLBT–2 thin films the fractal dimensionality remains virtually unchangeable at 2.30, whereas the BNLBT–3 sample revealed a higher D value, being around 2.43. Thus, the obtained values for the fractal dimensionality are in good agreement with the experimental values reported for PZT ferroelectric thin films (2.42–2.49), with thicknesses between 50 and 91 nm,[91] with an expected theoretical value for D around 2.50.[92]

To investigate the boundaries between different contrasted regions upward and downward polarized ferroelectric domains randomly distributed in the layers, the quantitative characterization of domain-wall roughness was now considered. The correlation function B(L) of relative displacements was used to find the characteristic exponent of roughness (ξ) via the $B(L) \propto L^{2\xi}$ relation. Figure 9(c) shows the typical ln-ln plot of the correlation function B(L) and the fitting of the linear part of the curve, yielding the exponent (ξ) for the BNLBT–0 composition. Result reveals the ξ value to be around 0.60 ± 0.04. A similar result has also been found for the BNLBT–2 composition, whereas a lower value was observed for the BNLBT–3 sample (0.40 ± 0.02). The expected theoretical value for ξ (~ 3/5) is comparable to the reported values for two-dimensional domain-walls in materials with random local-fields.[93] In this scenario, the defects can promote a local asymmetry in the ferroelectric double-well potential and, therefore, a nonlinear creep response. From the presented results, it is possible to find a fundamental parameter for describing the speed of domains-wall motion in ferroelectric

materials. Under low electric field levels, below the threshold value (E_0) in the creep regime, the electric field dependence of the domain-wall speed can be described by the $v \propto exp\left[-R/k_BT\left(E_0/E\right)^{\mu}\right]$ relation, where R is the energy barrier and μ is a dynamical exponent, which reflects the nature of the system.[94] Indeed, the dynamical exponent is related to the roughness exponent through the relation expressed by the Equation (2).

$$\mu = \frac{D-2+2\xi}{2-\xi} \quad (2)$$

Thus, by using the values previously found for D and ξ, it was possible to obtain μ coefficient values around 1.08, 1.06 and 0.77 for the BNLBT–0, BNLBT–2 and BNLBT–3 compositions, respectively. Dynamical exponent values from 1.01 to 1.21 have been reported for $Pb(Zr_{0.20}Ti_{0.80})O_3$ thin films with different thicknesses,[94] which confirm the agreement between the obtained results in the present work with those reported in the literature. Other studies carried out in thin films have also investigated the influence of the defects purposely generated during crystal growth (or introduced by heavy ion irradiation) and the results revealed a decrease in the creep exponent, with the increase of the defects.[93] In this context, according to the results shown in Figure 8, the asymmetric nanoscale loops observed for the studied compositions in the present work, is a clear evidence of the defect dipoles (or defect clusters) induced by the pinning effect of domain-walls. Under a pinning potential, in the random field scenario, a dynamical exponent (μ) value close to 1.0 is expected. In addition, it has been observed that the μ exponent significantly drops with the increase of the lanthanum concentration for the studied BNLBT–*x* films. Therefore, the increase in the lanthanum concentration promotes an increase in the structural disorder, probably originated from the local quenched defects, thus confirming the obtained results for the fractal dimension. However, it is

important to emphasize that the understanding of the main role of polar nanoregions in the studied material continues to be a challenge up today.

4. CONCLUSIONS

$Bi_{0.506}Na_{0.46}Ba_{0.08-3x/2}La_xTiO_3$ (x = 0, 2 and 3 at%) lead-free thin films were successfully synthesized by a sol-gel method and deposited on $Pt(111)/TiO_2/SiO_2/Si$ substrate by the spin-coating technique. The expected perovskite structure was achieved and the coexistence between the antiferroelectric (tetragonal, P4*bm*) and ferroelectric (rhombohedral, R3*c*) phases was confirmed from XRD measurements and Raman spectroscopy, thus revealing the quality of the obtained thin films. Dense and crack-free nanostructured surface for the studied compositions was evaluated from the AFM surface topography. The increase of the lanthanum concentration has provided a decrease of both the grains size and the surface roughness. The PFM analysis has evidenced the piezo-/ferroelectric nature of the BNLBT–x thin films at the nanoscale, with a homogeneous piezo-activity for each film and a higher electromechanical response detected for the doped BNLBT films. The coercive voltage values V_C was also found to be much lower for the undoped film compared to the La^{3+} modified samples. The estimated effective piezoelectric constant for the pure sample was d_{33eff} ~ 34 pm/V, also revealing an enhanced local piezo-activity with the increase of the La content, thus suggesting the potential of the lead-free BNLBT thin films to replace lead-based materials. The nanodomain structure nature revealed long-range average correlation lengths for La-doped thin films, whereas the evaluation of the dynamic exponent, which describes the electric field dependence of the domain-wall speed, showed an increase and a decrease in the fractal dimension and exponent of roughness, respectively, with the increase of the doping content. This result confirms an increase in the structural disorder, probably originated from the local quenched defects, promoted by the increase of the lanthanum concentration. The nanoscale analysis of the domain wall revealed an intrinsic dependence of the dynamic coefficient that reflects the nature of the system, with

the increase of the lanthanum content, which indeed seems to be the main responsible for the local fields induced structural disorder.

ACKNOWLEDGMENTS

The authors thank the National Council of Scientific and Technological Development (CNPq) grant 303314/2016-8, Minas Gerais Research Foundation (FAPEMIG) grants PPM-00661-16 and APQ-02875-18 and Coordenação de Aperfeiçoamento de Pessoal de Nível Superior - Brasil (CAPES) - Finance Code 001 Brazilian agencies for the financial support. The Abdus Salam International Centre for Theoretical Physics, Trieste-Italy, for financial support of Latin-American Network of Ferroelectric Materials (NT-02) is also acknowledged. Dr. Mendez-González acknowledges the partial financial support by the ICTP-CLAF agreement AF-13. Thanks to the PHC "Carlos J. Finlay" (Project France-Cuba, 2017-2018). Région Hauts-de-France and Fonds Européen de Développement Régional (FEDER) are gratefully acknowledged for funding the MFP-3D microscope under Program "Chemistry and Materials for a Sustainable Growth". Chevreul Institute (FR 2638), Ministère de l'Enseignement Supérieur, de la Recherche et de l'Innovation, Hauts-de-France Region, Fonds Européen de Développement Régional (FEDER) and Major Domain of Interest (DIM) "Eco-Energy Efficiency" of Artois University are acknowledged for supporting and funding partially this work.

CONFLICTS OF INTEREST

There are no conflicts of interest to declare.

ORCID

J. D. S. Guerra https://orcid.org/0000-0002-7906-4343

REFERENCES

1. Uchino K, Ferroelectric devices. New York: Marcel and Dekker Inc.; 2000.
2. Rabe KM, Ahn CH, Triscone J-M. Physics of ferroelectrics. New York: Springer Berlin Heidelberg; 2007.
3. Saito Y, Takao H, Tani T, Nonoyama T, Takatori K, Homma T, Nagaya T, Nakamura M. Lead-free piezoceramics. Nature. 2004;432:84–7.
4. Zhang S, Li F. High performance ferroelectric relaxor-$PbTiO_3$ single crystals: Status and perspective. J Appl Phys. 2012;111:031301.
5. Yoon JG, Song TK. Fabrication and characterization of ferroelectric oxide thin films: in Handbook of thin films. Amsterdam: Elsevier; 2020.
6. Choi KJ, Biegalski M, Li YL, Sharan A, Schubert J, Uecker R, Reiche P, Chen YB, Pan XQ, Gopalan V, Chen L-Q, Schlom DG, Eom CB. Enhancement of ferroelectricity in strained $BaTiO_3$ thin films. Science. 2004;306:1005–09.
7. Schwarzkopf J, Fornari R. Epitaxial growth of ferroelectric oxide films. Prog Cryst Growth Charact Mater. 2006;52:159–212.
8. Du H, Tang F, Liu D, Zhu D, Zhou W, Qu S. The microstructure and ferroelectric properties of $(K_{0.5}Na_{0.5})NbO_3$–$LiNbO_3$ lead-free piezoelectric ceramics. Mater Sci Eng B. 2007;136:165–69.
9. Liu W, Ren X. Large piezoelectric effect in Pb-free ceramics. Phys Rev Lett. 2009;103:257602.
10. Nanamatsu S, Kimura M, Doi K, Takahashi M. Ferroelectric properties of $Sr_2Nb_2O_7$ single crystal. J Phys Soc Jpn. 1971;30:300–01.

11. Kimura M, Nanamatsu S, Kawamura T, Matsushita S. Ferroelectric, electrooptic and piezoelectric properties of $Nd_2Ti_2O_7$ single crystal. Jpn J Appl Phys. 1974;13:1473–74.
12. Bayart A, Saitzek S, Chambrier M-H, Shao Z, Ferri A, Huvé M, Pouhet R, Tebano A, Roussel P, Desfeux R. Microstructural investigations and nanoscale ferroelectric properties in lead-free $Nd_2Ti_2O_7$ thin films grown on $SrTiO_3$ substrates by pulsed laser deposition. CrystEngComm. 2013;15:4341–50.
13. Kato K, Zheng C, Finder JM, Dey SK. Sol-gel route to ferroelectric layer-structured perovskite $SrBi_2Ta_2O_9$ and $SrBi_2Nb_2O_9$ thin films. J Am Ceram Soc. 1998;81:1869–75.
14. Cummins SE, Cross LE. Electrical and optical properties of ferroelectric $Bi_4Ti_3O_{12}$ single crystals. J Appl Phys. 1968;39:2268–74.
15. Glass AM. Investigation of the electrical properties of $Sr_{1-x}Ba_xNb_2O_6$ with special reference to pyroelectric detection. J Appl Phys. 1969;40:4699–13.
16. Singh S, Levinstein HJ, Van Uitert LG. Role of hydrogen in polarization reversal of ferroelectric $Ba_2NaNb_5O_{15}$. Appl Phys Lett. 1970;16:176–78.
17. Carlier T, Chambrier M-H, Ferri A, Estradé S, Blach J-F, Martín G, Meziane B, Peiró F, Roussel P, Ponchel F, Rèmiens D, Cornet A, Desfeux R. Lead-free α-La_2WO_6 ferroelectric thin films. ACS Appl Mater Inter. 2015;7:24409−18.
18. Carlier T, Chambrier M-H, Da Costa A, Blanchard F, Denneulin T, Létiche M, Roussel P, Desfeux R, Ferri A. Ferroelectric state in a α-Nd_2WO_6 polymorph stabilized in thin film. Chem Mater. 2020;32:7188–00.
19. Zhang ST, Kounga AB, Aulbach E, Granzow T, Jo W, Kleebe HJ, Rödel J. Lead-free piezoceramics with giant strain in the system $Bi_{0.5}Na_{0.5}TiO_3$–$BaTiO_3$–$K_{0.5}Na_{0.5}NbO_3$. I. Structure and room temperature properties. J Appl Phys. 2008;103:034107.

20. Cordero F, Craciun F, Trequattrini F, Mercadelli E, Galassi C. Phase transitions and phase diagram of the ferroelectric perovskite $(Na_{0.5}Bi_{0.5})_{1-x}Ba_xTiO_3$ by anelastic and dielectric measurements. Phys Rev B. 2010;81:144124
21. Coondoo I, Panwar N, Kholkin A. Lead–free piezoelectrics: Current status and perspectives. J Adv Dielectr. 2013;3:1330002.
22. Takenaka T, Maruyama K, Sakata K. $(Bi_{1/2}Na_{1/2})TiO_3$–$BaTiO_3$ system for lead–free piezoelectric ceramics. Jpn J Appl Phys. 1991;30:2236–39.
23. Ma C, Tan X, Dul'kin E, Roth M. Domain structure-dielectric property relationship in lead-free $(1-x)Bi_{1/2}Na_{1/2}TiO_3-xBaTiO_3$ ceramics. J Appl Phys. 2010;108:104105.
24. Cao J, Wang Y, Li Z. Effect of La doping on the electrical behaviors of BNT–BT based ceramics. Ferroelectrics. 2017;520:224–30.
25. Shrout TR, Zhang SJ. Lead-free piezoelectric ceramics: Alternatives for PZT?. J Electroceram. 2007;19:113–26.
26. Kundu S, Maurya D, Clavel M, Zhou Y, Halder NN, Hudait MK, Banerji P, S. Priya S. Integration of lead-free ferroelectric on HfO_2/Si (100) for high performance non-volatile memory applications. Sci Rep. 2015;5:8494.
27. Schwartz RW, Schneller T, Waser R. Chemical solution deposition of electronic oxide films. C R Chimie. 2004;7:433–61.
28. Christensen M, Einarsrud MA, Grande T. Fabrication of lead-free $Bi_{0.5}Na_{0.5}TiO_3$ thin films by aqueous chemical solution deposition. Materials 2017;10:213–29.
29. Zheng XC, Zheng GP, Lin Z, Jiang ZY. Thermo-electrical energy conversions in $Bi_{0.5}Na_{0.5}TiO_3$–$BaTiO_3$ thin-films prepared by sol–gel method. Thin Solid Films. 2012;522:125–28.
30. Cernea M, Galca AC, Cioangher MC, Dragoi C, Ioncea G. Piezoelectric BNT–$BT_{0.11}$ thin-films processed by sol–gel technique. J Mater Sci. 2011;46:5621–27.

31. Cernea M, Trupina L, Dragoi C, Vasile BS, Trusca R. Structural and piezoelectric characteristics of BNT–$BT_{0.05}$ thin films processed by sol–gel technique. J Alloys Compd. 2012;515:166–70.
32. Cernea M, Trupina L, Dragoi C, Galca AC, Trinca L. Structural, optical, and electric properties of BNT–$BT_{0.08}$ thin-films processed by sol–gel technique. J Mater Sci. 2012;47:6966–71.
33. Acharya SK, Lee SK, Hyung JH, Yang YH, Kim BH, Ahn BG. Ferroelectric and piezoelectric properties of lead-free $BaTiO_3$ doped $Bi_{0.5}Na_{0.5}TiO_3$ thin-films from metal-organic solution deposition. J Alloys Compd. 2012;540:204–09.
34. Yu T, Kwok KW, Chan HLW. The synthesis of lead-free ferroelectric $Bi_{0.5}Na_{0.5}TiO_3$–$Bi_{0.5}K_{0.5}TiO_3$ thin films by sol–gel method. Mater Lett. 2007;61:2117–20.
35. Wu Y, Wang X, Zhong C, Li L. Effect of Na/K excess on the electrical properties of $Na_{0.5}Bi_{0.5}TiO_3$–$K_{0.5}Bi_{0.5}TiO_3$ thin films prepared by sol–gel processing. Thin Solid Films 2011;519:4798–03.
36. Mendez-González Y, Peláiz-Barranco A, Guerra JDS, Penton-Madrigal A, Saint-Grégoire P. Effect of the lanthanum concentration on the physical properties of the $(Bi_{0.5}Na_{0.5})_{0.92}Ba_{0.08-3x/2}La_xTiO_3$ ceramic system. Mater Chem Phys. 2018;208:103–11.
37. Mendez-González Y, Peláiz-Barranco A, Curcio AL, Rodrigues AD, Guerra JDS. Raman spectroscopy study of the La-modified $(Bi_{0.5}Na_{0.5})_{0.92}Ba_{0.08}TiO_3$ lead-free ceramic system. J Raman Spect. 2019;50:1044–50.
38. Mendez-González Y, Peláiz-Barranco A, Guerra JDS. Improved electrocaloric properties in La doped $(Bi_{0.5}Na_{0.5})_{0.92}Ba_{0.08}TiO_3$ lead-free ceramics. Appl Phys Lett. 2019;114:162902.
39. Li L, Xu M, Zhang Q, Chen P, Peng B, Liu L. Electrocaloric effect in La-doped BNT–6BT relaxor ferroelectric ceramics. Ceram Int. 2018;44:343–50.

40. Gruverman A, Kalinin SV. Piezoresponse force microscopy and recent advances in nanoscale studies of ferroelectrics. J Mater Sci. 2006;41:107–16.
41. Gruverman A, Alexe M, Meier D. Piezoresponse force microscopy and nanoferroic phenomena. Nat Commun. 2019;10:1661.
42. Larson AC, Von Dreele RB. General Structure Analysis System (GSAS). Los Alamos National Laboratory Report LAUR. 1994:86–748
43. Toby BH. *EXPGUI*, a graphical user interface for *GSAS*. J Appl Cryst. 2001;34,210–13.
44. Thompson P, Cox DE, Hastings JB. Rietveld refinement of Debye-Scherrer synchrotron X-ray data from Al_2O_3. J Appl Cryst. 1987;20:79–83
45. Rodriguez BJ, Callahan C, Kalinin SV, Proksch R. Dual-frequency resonance-tracking atomic force microscopy. Nanotechnology. 2007;18:475504.
46. Jones GO, Thomas PA. The tetragonal phase of $Na_{0.5}Bi_{0.5}TiO_3$ - a new variant of the perovskite structure. Acta Cryst B. 2000;56:426–30.
47. Jones GO, Thomas PA. Investigation of the structure and phase transitions in the novel A-site substituted distorted perovskite compound $Na_{0.5}Bi_{0.5}TiO_3$. Acta Cryst B. 2002;58:168–78.
48. Davey WP. Precision measurements of the lattice constants of twelve common metals. Phys Rev. 1925;25:753–61.
49. Pertsev NA, Zembilgotov AG, Tagantsev AK. Effect of mechanical boundary conditions on phase diagrams of epitaxial ferroelectric thin films. Phys Rev Lett. 1998;80:1988–91.
50. Guerra JDS, Mendes RG, Eiras JA, Santos IA, Araújo EB. Investigation of nonlinear dielectric properties in relaxor ferroelectric thin films. J Appl Phys. 2008;103:014102.
51. Hector AL, Wiggin SB. Synthesis and structural study of stoichiometric $Bi_2Ti_2O_7$ pyrochlore. J Solid State Chem. 2004;177:139–45.
52. Inorganic Crystal Structure Database (ICSD-2014), FIZ Karlsruhe, Germany.

53. Birkholz M. Thin film analysis by X-ray scattering. Weinheim: Wiley-VCH; 2006.
54. Liu X, Guo H, Tan X. Evolution of structure and electrical properties with lanthanum content in $[(Bi_{1/2}Na_{1/2})_{0.95}Ba_{0.05}]_{1-x}La_xTiO_3$ ceramics. J Eur Ceram Soc. 2014;34:2997–06.
55. Kreisel J, Glazer AM, Jones G, Thomas PA, Abello L, Lucazeau G. An X-ray diffraction and Raman spectroscopy investigation on A-site substituted perovskite compounds: the $(Na_{1-x}K_x)_{0.5}Bi_{0.5}TiO_3$ ($0<x<1$) solid solution. J Phys: Condens Matter. 2000;12:3267–80.
56. Pal V, Thakur OP, Dwivedi RK. Investigation of MPB region in lead free BLNT–BCT system through XRD and Raman spectroscopy. J Phys D: Appl Phys. 2015;48:055301.
57. Shi J, Fan H, Liu X, Bell AJ. Large electrostrictive strain in $(Bi_{0.5}Na_{0.5})TiO_3$–$BaTiO_3$–$(Sr_{0.7}Bi_{0.2})TiO_3$ solid solutions. J Am Ceram Soc. 2014;97:848–53.
58. Buixaderas E, Gregora I, Savinov M, Hlinka J, Jin L, Damjanovic D, Malic B. Compositional behavior of Raman-active phonons in $Pb(Zr_{1-x}Ti_x)O_3$ ceramics. Phys Rev B. 2015;91:014104.
59. Ting CJ, Peng CJ, Lu HY, Wu ST. Lanthanum-Magnesium and lanthanum-Manganese Donor-Acceptor-Codoped Semiconducting Barium Titanate. J Am Ceram Soc. 1990;73:329–34.
60. Desfeux R, Legrand C, Da Costa A, Chateigner D, Bouregba R, Poullain G. Correlation between local hysteresis and crystallite orientation in PZT thin films deposited on Si and MgO substrates. Surf Sci. 2006;600:219–28.
61. Ferri A, Da Costa A, Desfeux R, Detalle M, Wang GS, Remiens D. Nanoscale investigations of electrical properties in relaxor $Pb(Mg_{1/3}Nb_{2/3})O_3$–$PbTiO_3$ thin films deposited on platinum and $LaNiO_3$ electrodes by means of local piezoelectric response. Integr Ferroelectr. 2007;91:80–96.
62. Ferri A, Da Costa A, Saitzek S, Desfeux R, Detalle M, Wang GS, Remiens D. Local piezoelectric hysteresis loops for the study of electrical properties of $0.7Pb(Mg_{1/3}Nb_{2/3})O_3$–

0.3$PbTiO_3$ thin films: bottom electrode dependence and film thickness effects. Ferroelectrics. 2008;362:21–29.

63. Liu Y, Weiss DN, Li J. Rapid nanoimprinting and excellent piezoelectric response of polymer ferroelectric nanostructures. ACS Nano. 2010;4:83–90.
64. Abou Dargham S, Ponchel F, Abboud N, Soueidan M, Ferri A, Desfeux R, Assaad J, Remiens D, Zaouk D. Synthesis and electrical properties of lead-free piezoelectric $Bi_{0.5}Na_{0.5}TiO_3$ thin films prepared by Sol-Gel method. J Eur Ceram Soc. 2018;38:1450–55.
65. Boldyreva K, Bao D, Le Rhun G, Pintilie L, Alexe M, D. Hesse D. Microstructure and electrical properties of $(120)_O$-oriented and of $(001)_O$-oriented epitaxial antiferroelectric $PbZrO_3$ thin films on (100) $SrTiO_3$ substrates covered with different oxide bottom electrodes. J Appl Phys. 2007;102:044111.
66. Chaudhuri AR, Arredondo M, Hähnel A, Morelli A, Becker M, Alexe M, Vrejoiu I. Epitaxial strain stabilization of a ferroelectric phase in $PbZrO_3$ thin films. Phys Rev B. 2011;84:054112.
67. Martin D, Müller J, Schenk T, Arruda TM, Kumar A, Strelcov E, Yurchuk E, Müller S, Pohl D, Schröder U, Kalinin SV, Mikolajick T. Ferroelectricity in Si-doped HfO_2 revealed: A binary lead-free ferroelectric. Adv Mater. 2014;26:8198–02.
68. Lu, H, Glinsek S, Buragohain P, Defay E, Iñiguez J, Gruverman A. Probing Antiferroelectric-Ferroelectric Phase Transitions in $PbZrO_3$ Capacitors by Piezoresponse Force Microscopy. Adv Funct Mater. 2020;2020:2003622.
69. Ferri A, Saitzek S, Da Costa A, Desfeux R, Leclerc G, Bouregba R, G. Poullain G. Thickness dependence of the nanoscale piezoelectric properties measured by piezoresponse force microscopy on (111)-oriented PLZT 10/40/60 thin films. Surf. Sci. 2008;602:1987–92.

70. Lichtensteiger C, Fernandez-Pena S, Weymann C, Zubko P, Triscone J-M. Tuning of the depolarization field and nanodomain structure in ferroelectric thin films. Nano Lett. 2014;14:4205–11.
71. Okazaki K, Nagata K. Effects of grain size and porosity on electrical and optical properties of PLZT ceramics. J Am Ceram Soc. 1973;56:82–86.
72. Grossmann M, Lohse O, Bolten D, Boettger U, Schneller T, Waser R. The interface screening model as origin of imprint in thin films. I. Dopant, illumination, and bias dependence. J Appl Phys. 2002;92:2680–87.
73. Carl K, Hardtl KH. Electrical after-effects in $Pb(Ti,Zr)O_3$ ceramic. Ferroelectrics. 1978;17:473–86.
74. Arlt G, Neumann H. Internal bias in ferroelectric ceramics: origin and time dependence. Ferroelectrics. 1988;87:109–20.
75. Dimos D, Warren WL, Sinclair MB, Tuttle BA, Schwartz RW. Photoinduced hysteresis changes and optical storage in $(Pb,La)(Zr,Ti)O_3$ thin films and ceramics. J Appl Phys. 1994;76:4305–15.
76. Warren WL, Tuttle BA, Dimos D, Pike GE, Al-Shareef HN, Ramesh R, Evans JT. Imprint in ferroelectric capacitors. Jpn J Appl Phys. 1996;35(2S):1521–24.
77. Eyraud L, Eyraud P, Claudel B. Influence of simultaneous heterovalent substitutions in both cationic sites on the ferroelectric properties of PZT type ceramics. J Solid State Chem. 1984;53:266–72.
78. Ang C, Yu Z, Cross LE. Oxygen-vacancy-related low-frequency dielectric relaxation and electrical conduction in $Bi:SrTiO_3$. Phys Rev B. 2000;62:228–36.
79. Pike GE, Warren WL, Dimos D, Tuttle BA, Ramesh R, Lee J, Keramidas VG, Evans JT. Voltage offsets in $(Pb,La)(Zr,Ti)O_3$ thin films. Appl Phys Lett. 1995;66:484–86.

80. Yueqiu G, Hui D, Xuejun Z, Jinfeng P, Xujun L, H. Renjie H. Large piezoelectric response of $Bi_{0.5}(Na_{(1-x)}K_x)_{0.5}TiO_3$ thin films near morphotropic phase boundary identified by multi-peak fitting. J Phys D: Appl Phys. 2012;45:305301.
81. Necas D, Klapetek P. Gwyddion: an open-source software for SPM data analysis. Cent Eur J Phys. 2012;10:181–88.
82. Shvartsman VV, Dkhil B, Kholkin AL. Mesoscale domains and nature of the relaxor state by piezoresponse force microscopy. Annu Rev Mater Res. 2013;43:423–49.
83. Melo M, Araújo EB, Shvartsman VV, Shur VYa, Kholkin AL. Thickness effect on the structure, grain size, and local piezoresponse of self-polarized lead lanthanum zirconate titanate thin films. J Appl Phys. 2016;120:054101.
84. Daniels JE, Jo W, Rödel J, Daniel Rytz D, Donner W. Structural origins of relaxor behavior in a $0.96(Bi_{1/2}Na_{1/2})TiO_3$–$0.04BaTiO_3$ single crystal under electric field. Appl Phys Lett. 2011;98:252904.
85. Bokov AA, Ye Z-G. Recent progress in relaxor ferroelectrics with perovskite structure. J Mater Sci. 2006;41:31–52.
86. Ishibashi Y, Takagi Y. Note on ferroelectric domain switching. J Phys Soc Jpn. 1971;31:506–10.
87. Mitic VV, Lazovic G, Paunovic V, Cvetkovic N, Jovanovic D, Veljkovic S, Randjelovic B, Vlahovic B. Fractal frontiers in microelectronic ceramic materials. Ceram Int. 2019;45:9679–85.
88. Mitic VV, Lazovic G, Paunovic V, Hwu RJ, Tsay S-Ch, Perng T-P, Veljkovic S, Vlahovic B. Ceramic materials and energy – Extended Coble's model and fractal nature. J Eur Ceram Soc. 2019;39:3513–25.
89. Mitic VV, Lazovic G, Lu C-An, Paunovic V, Radovic I, Stajcic A, Vlahovic B. The nano-scale modified $BaTiO_3$ morphology influence on electronic properties and ceramics fractal nature frontiers. Appl Sci. 2020;10:3485.

90. Douketis C, Wang Z, Haslett TL, Moskovits M. Fractal character of cold-deposited silver films determined by low-temperature scanning tunneling microscopy. Phys Rev B. 1995;51:11022–31.
91. Paruch P, Giamarchi T, Triscone J-M. Domain wall roughness in epitaxial ferroelectric $PbZr_{0.2}Ti_{0.8}O_3$ thin films. Phys Rev Lett. 2005;94:197601.
92. Scott JF. Absence of true critical exponents in relaxor ferroelectrics: the case for defect dynamics. J Phys: Condens Matter 2006;18:7123–34.
93. Paruch P, Giamarchi T, Tybell T, Triscone J-M. Nanoscale studies of domain wall motion in epitaxial ferroelectric thin films. J Appl Phys. 2006;100:051608.
94. Tybell T, Paruch P, Giamarchi T, Triscone J-M. Domain wall creep in epitaxial ferroelectric $Pb(Zr_{0.2}Ti_{0.8})O_3$ thin films. Phys Rev Lett. 2002;89:097601.

TABLES AND FIGURES CAPTIONS

Table 1. Unit-cell (*a*, *b* and *c*), volume (*V*) and goodness-of-fit (R_p, R_{wp} and χ^2) parameters obtained after the refinement process for all the compositions. Data for the resulting phases fractional weight (*w*) are also included. SG refers to the space group.

Table 2. Wavenumber (W) and assigned vibrational modes (VM) for the studied thin films (BNLBT–0, BNLBT–2 and BNLBT–3 compositions).

Figure 1. X-ray diffraction patterns of the studied BNLBT–*x* thin films, collected at room temperature. The cross-sectional SEM image for the BNLBT–2 composition, is also presented.

Figure 2. Rietveld refinement of the X-ray diffraction patterns for the BNLBT–0, BNLBT–2 and BNLBT–3 compositions (a, b and c, respectively). The experimental (observed) and theoretical (calculated profiles) data are represented by symbols and solid lines (in red), respectively. The vertical marks, below the patterns, correspond to the calculated Bragg's reflections. The differences between the experimental and theoretical data are identified by bottom blue lines.

Figure 3. (a) Composition (*x*) dependence of the lattice parameters for the tetragonal (a_T and c_T) and rhombohedral (a_R and c_R) phases for the studied thin films. The calculated phase fractions (*w*) as a function of the La content are also presented (b and c).

Figure 4. Raman spectra for the studied thin films (BNLBT–0, BNLBT–2 and BNLBT–3 compositions). The modes scripted by T and R are associated to the tetragonal and rhombohedral phases, respectively.

Figure 5. Measured Raman scattering spectra (open symbols), together with the fitted spectra (solid-lines) and the decomposed active modes (dashed-lines), for the studied thin films.

Figure 6. AFM topographic images of the films recorded over (a) 5×5 μm^2, (b) 2×2 μm^2 scan regions and (c) grain-size distributions for the different compositions: (i) BNLBT–0, (ii) BNLBT–2 and (iii) BNLBT–3.

Figure 7. As-grown OP amplitude (a, c and e) and phase (b, d and f) PFM patterns detected over the surfaces for the BNLBT–0 (a, b), BNLBT–2 (c, d) and BNLBT–3 (e, f) compositions.

Figure 8. Remnant phase (a, c and e) and amplitude (b, d and f) PFM loops recorded on the free surface of the films: BNLBT–0 (a, b), BNLBT–2 (c, d) and BNLBT–3 (e, f).

Figure 9. (a) Distance dependence of autocorrelation function for the BNLBT–0 thin film over all in-plane directions; the values are normalized to C($r=0$). (b) Average correlation length (Δ), fractal dimension of the "polarization interface", and roughness exponent (ξ) for the BNLBT–x thin films as a function of the La content (x). (c) Typical ln-ln plot of correlation function B(L) and fitting of the linear part of the curve yielding the exponent (ξ) for the BNLBT–0 composition. Line in (c) is drawn as a guide to the eye.

BNLBT–0							
SG	$a = b$ (Å)	c (Å)	V (Å^3)	w (%)	R_{wp}	R_p	χ^2
P4*bm*	5.518(1)	3.911(1)	119.10(5)	66.7(4)	0.0946	0.0706	1.353
R3*c*	5.491(3)	13.512(8)	352.8(3)	29.1(9)			
F$m\bar{3}m$	3.921(4)	–	60.3(1)	2.5(3)			
F$d\bar{3}m$	10.39(4)	–	1120(6)	1.7(3)			
BNLBT–2							
SG	$a = b$ (Å)	c (Å)	V (Å^3)	w (%)	R_{wp}	R_p	χ^2
P4*bm*	5.539(2)	3.904(3)	119.8(1)	53.7(5)	0.0945	0.0707	1.335
R3*c*	5.491(1)	13.525(7)	353.2(2)	39.6(6)			
F$m\bar{3}m$	3.918(2)	–	60.14(6)	4.3(1)			
F$d\bar{3}m$	10.388(2)	–	1121.0(3)	2.4(2)			
BNLBT–3							
SG	$a = b$ (Å)	c (Å)	V (Å^3)	w (%)	R_{wp}	R_p	χ^2
P4*bm*	5.510(2)	3.904(2)	118.51(9)	39.4(5)	0.1131	0.0856	2.346
R3*c*	5.4814(9)	13.500(5)	351.3(2)	44.5(5)			
F$m\bar{3}m$	3.903(1)	–	59.46(3)	15.1(3)			
F$d\bar{3}m$	10.39(3)	–	1121(6)	1.0(5)			

Table 1. Mendez-González et al.

Modes' Number	BNLBT–0	BNLBT–2	BNLBT–3	VM
	W (cm^{-1})			
M_1	–	116	119	$E(LO1)_T$ or $E(TO1)_R$
M_2	130	141	144	$A_1(TO1)_T$ or $A_1(TO1)_R$
M_3	238	237	224	$A_1(TO2)_T$ or $A_1(TO4)_R$
M_4	315	310	294	$E(LO2)_T + B_1$
M_5	500	505	511	$A_1(TO3)_T$ or $E(TO8)_R$
M_6	617	610	605	$A_1(TO8)_T$
M_7	776	773	773	$A_1(LO3)_T$ or $A_1(LO8)_R$
M_8	855	851	856	$E(LO3)_T$ or $A_1(LO9)_R$

Table 2. Mendez-González et al.

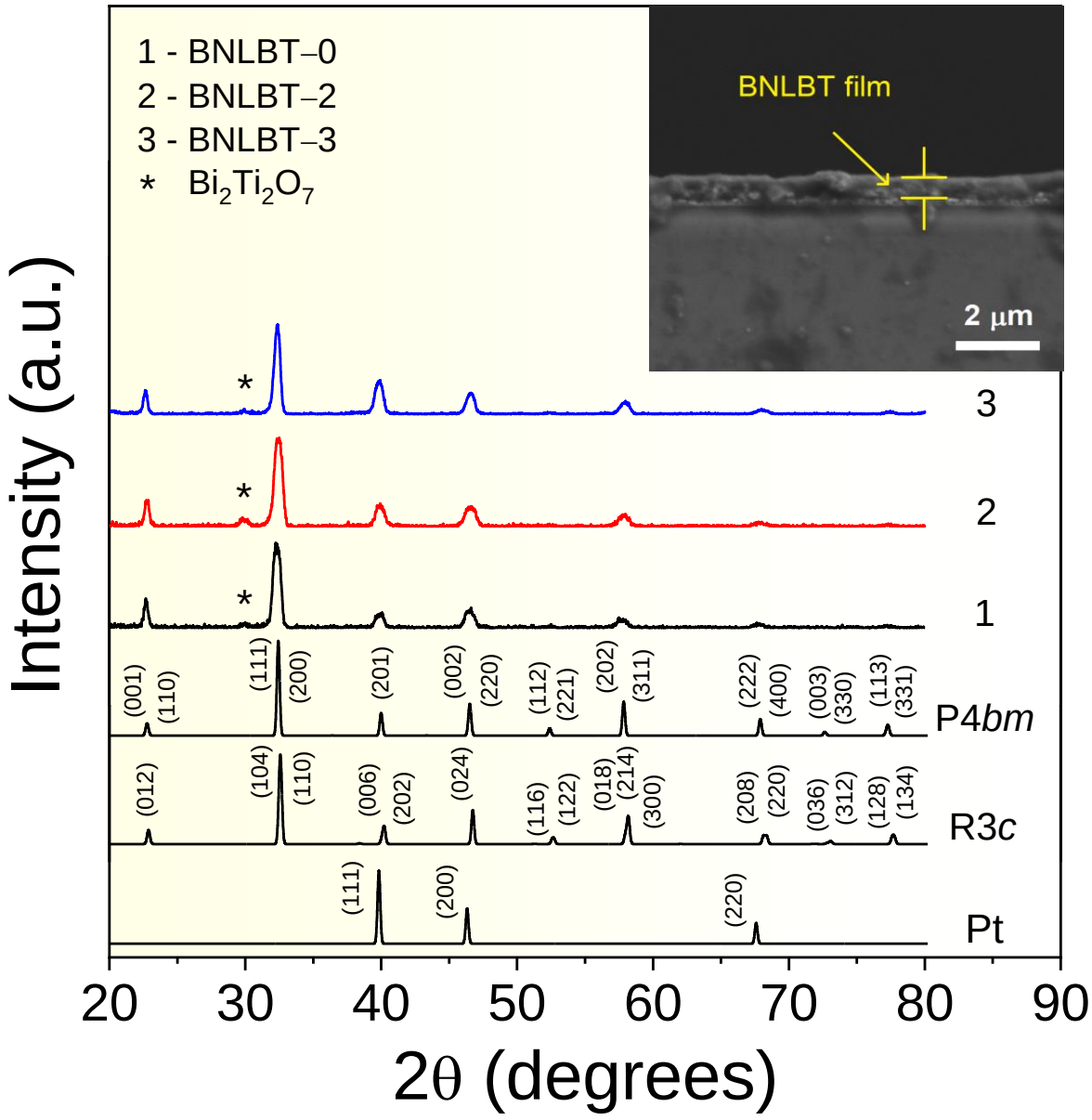

Figure 1. Mendez-González et al.

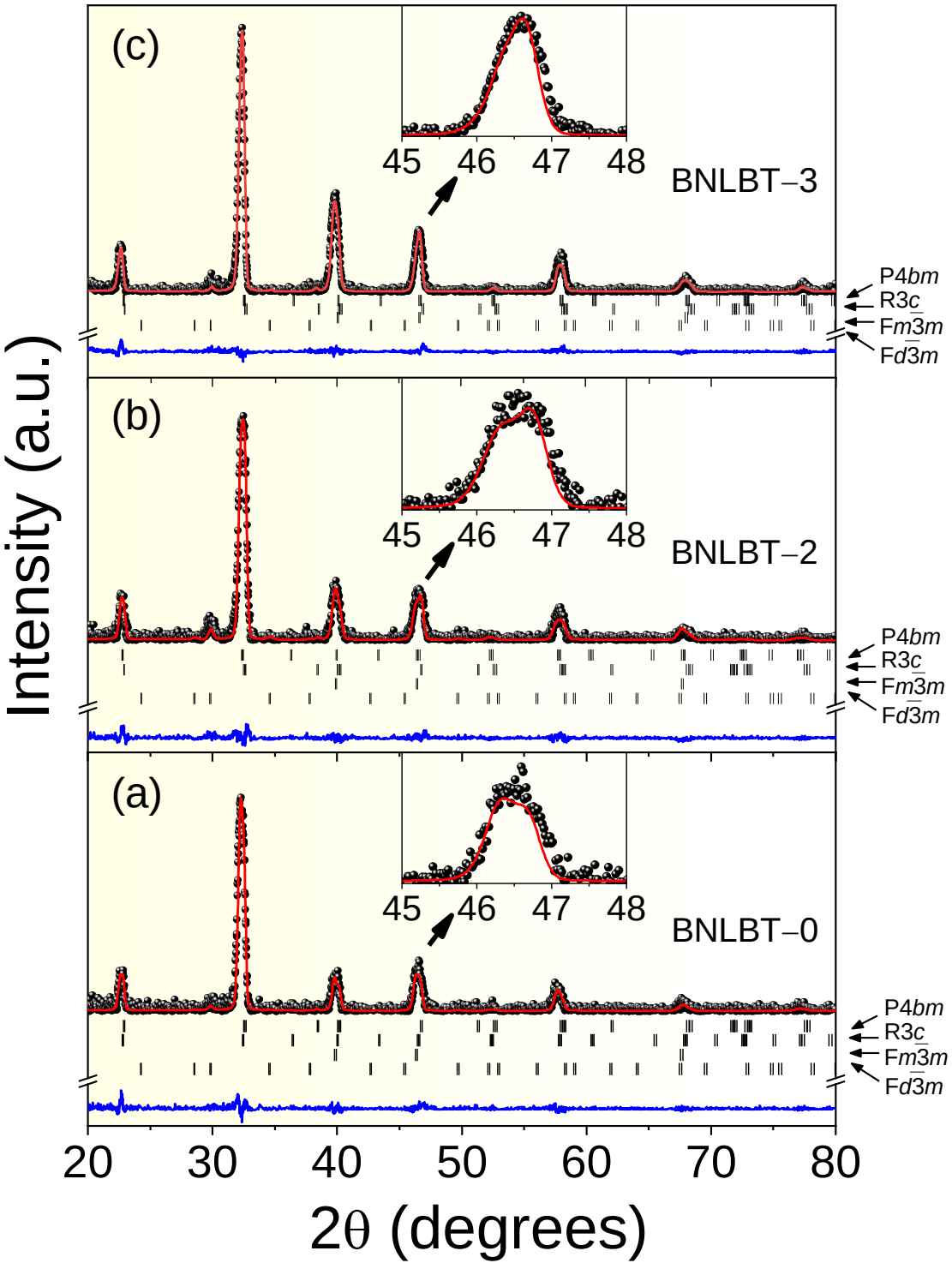

Figure 2. Mendez-González et al.

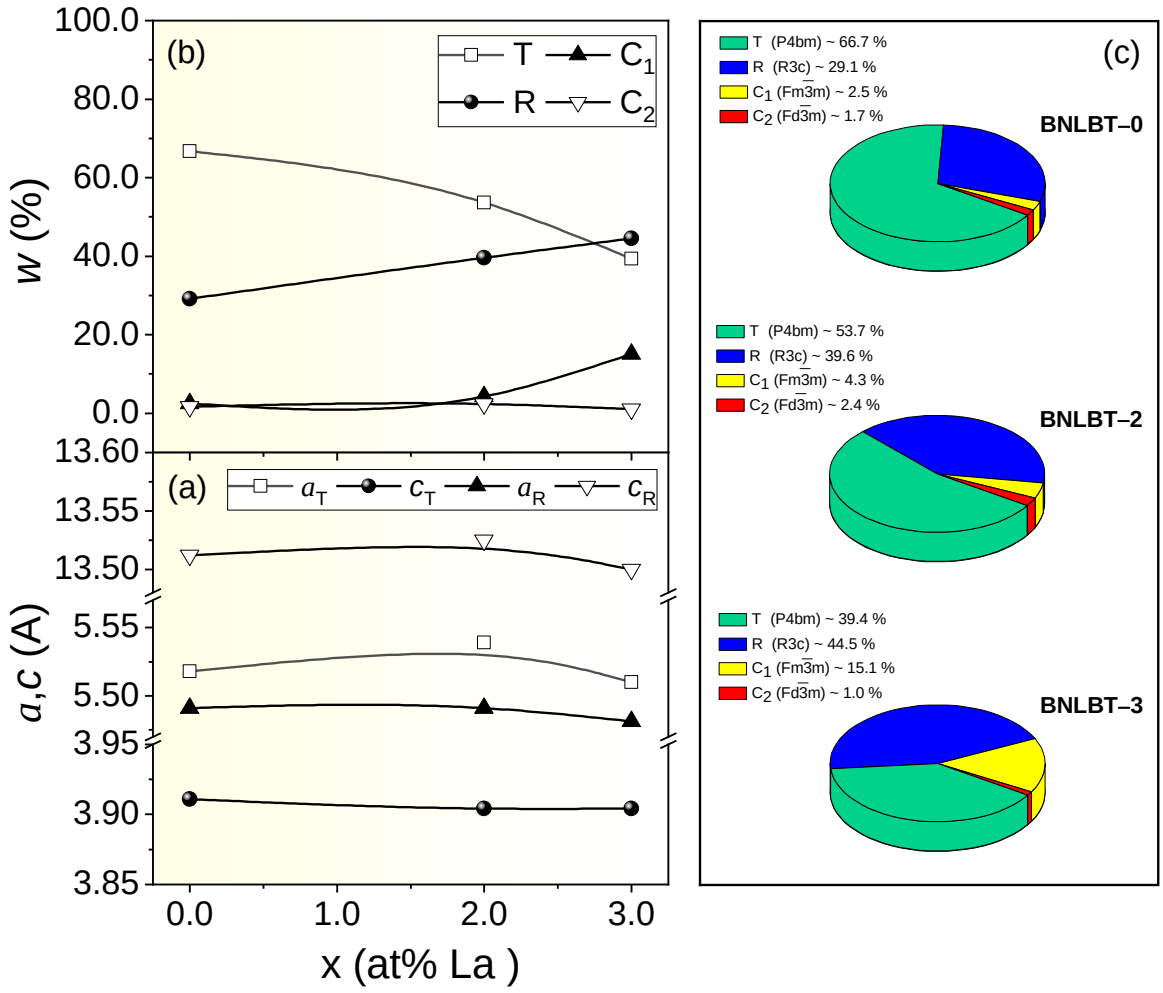

Figure 3. Mendez-González et al.

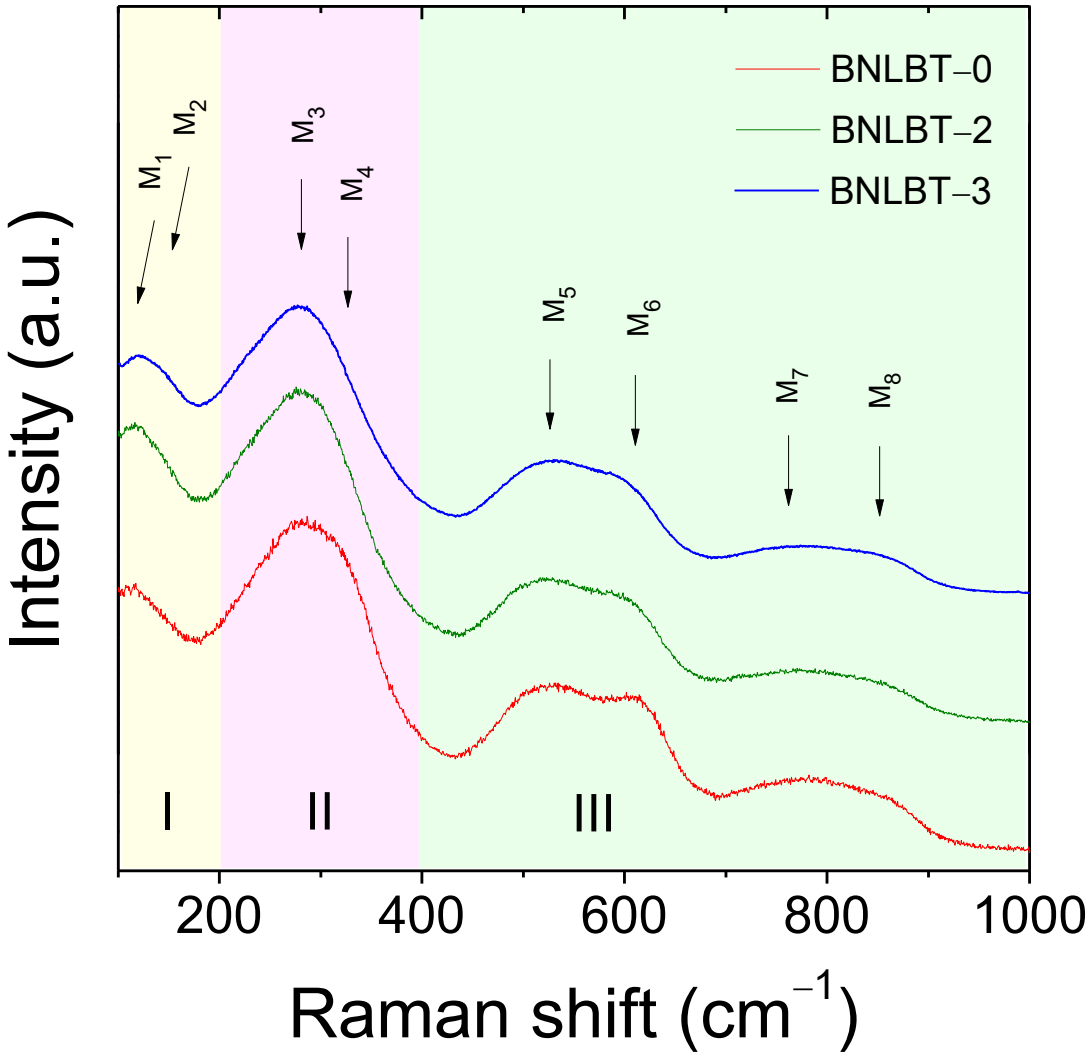

Figure 4. Mendez-González et al.

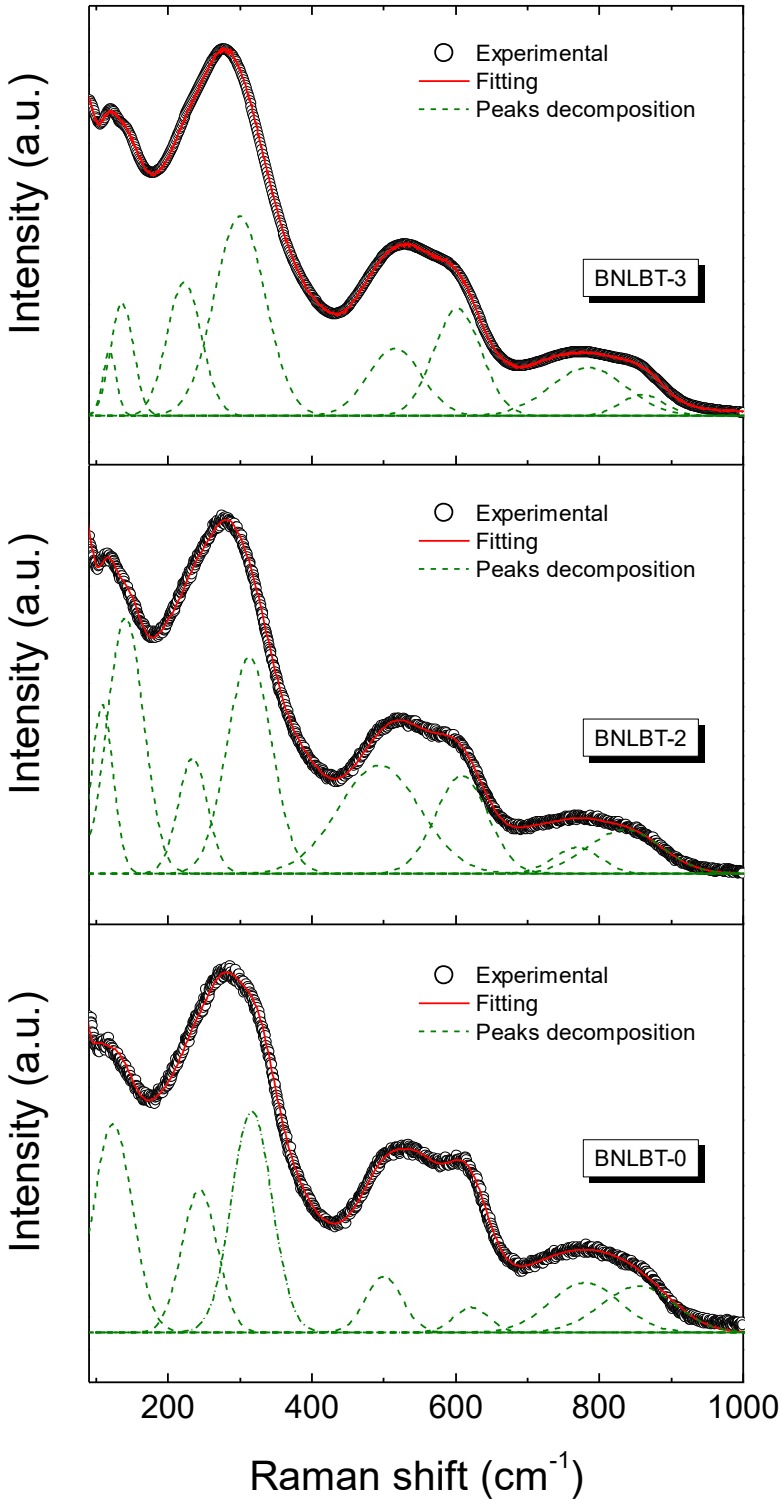

Figure 5. Mendez-González et al.

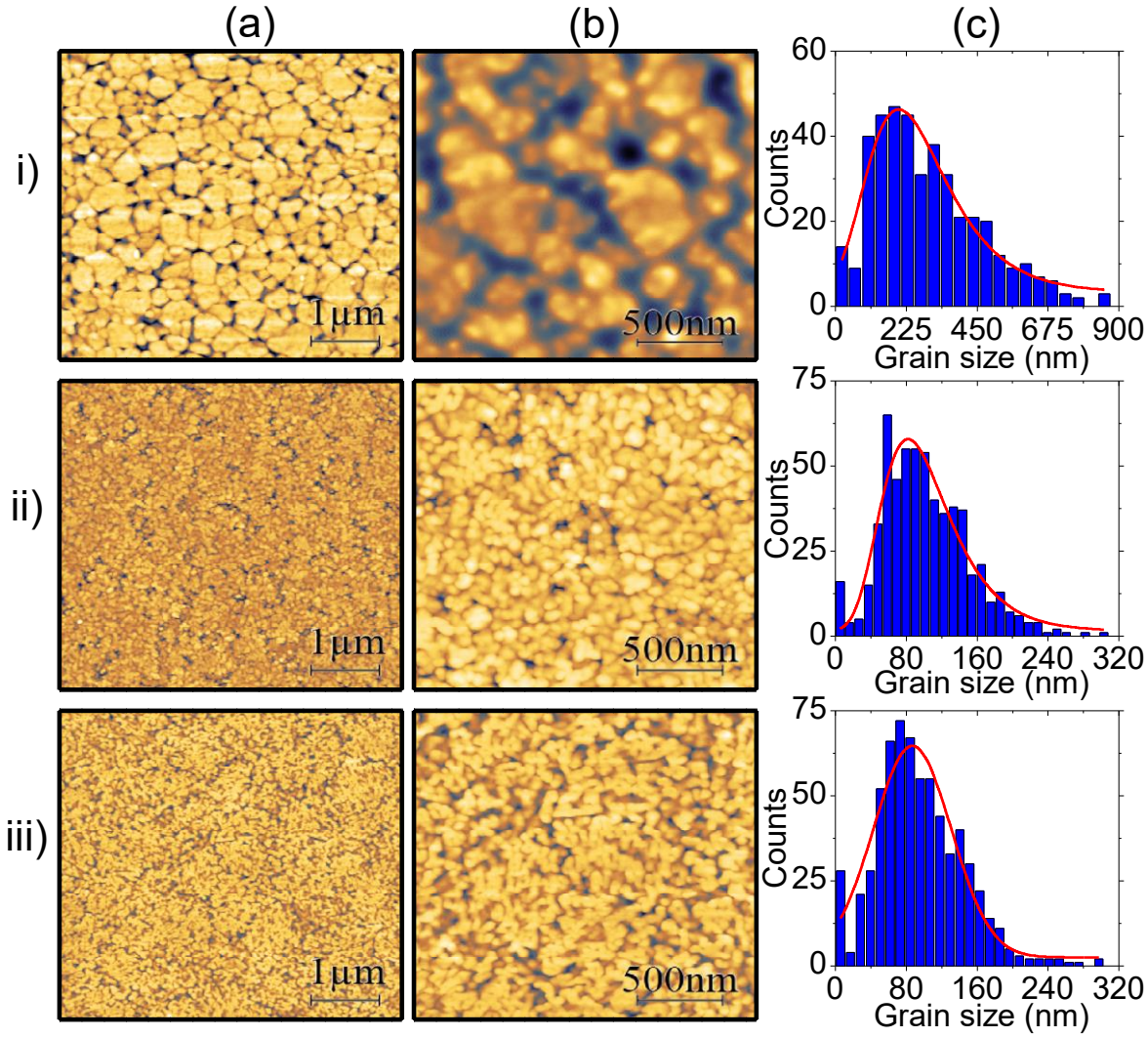

Figure 6. Mendez-González et al.

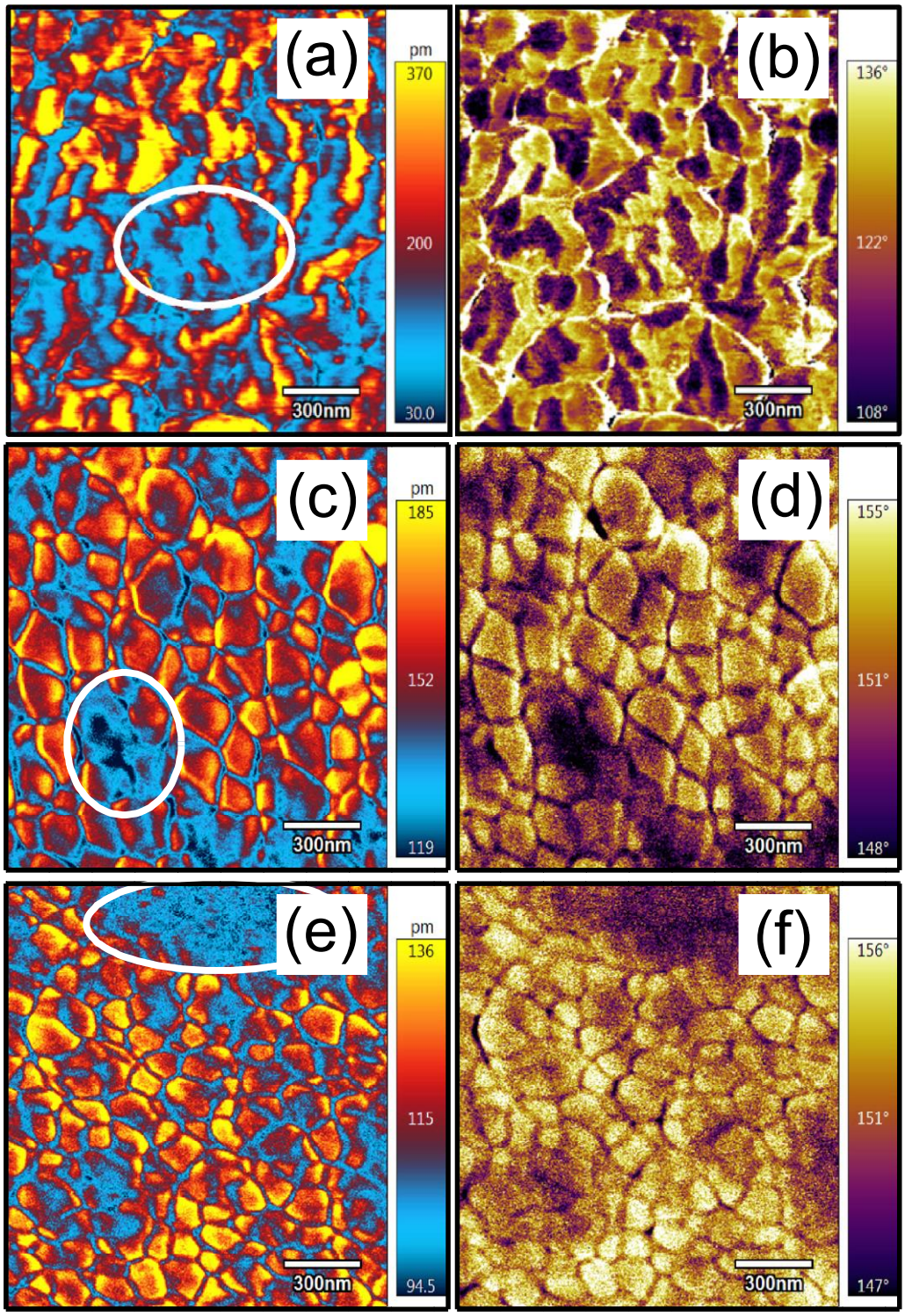

Figure 7. Mendez-González et al.

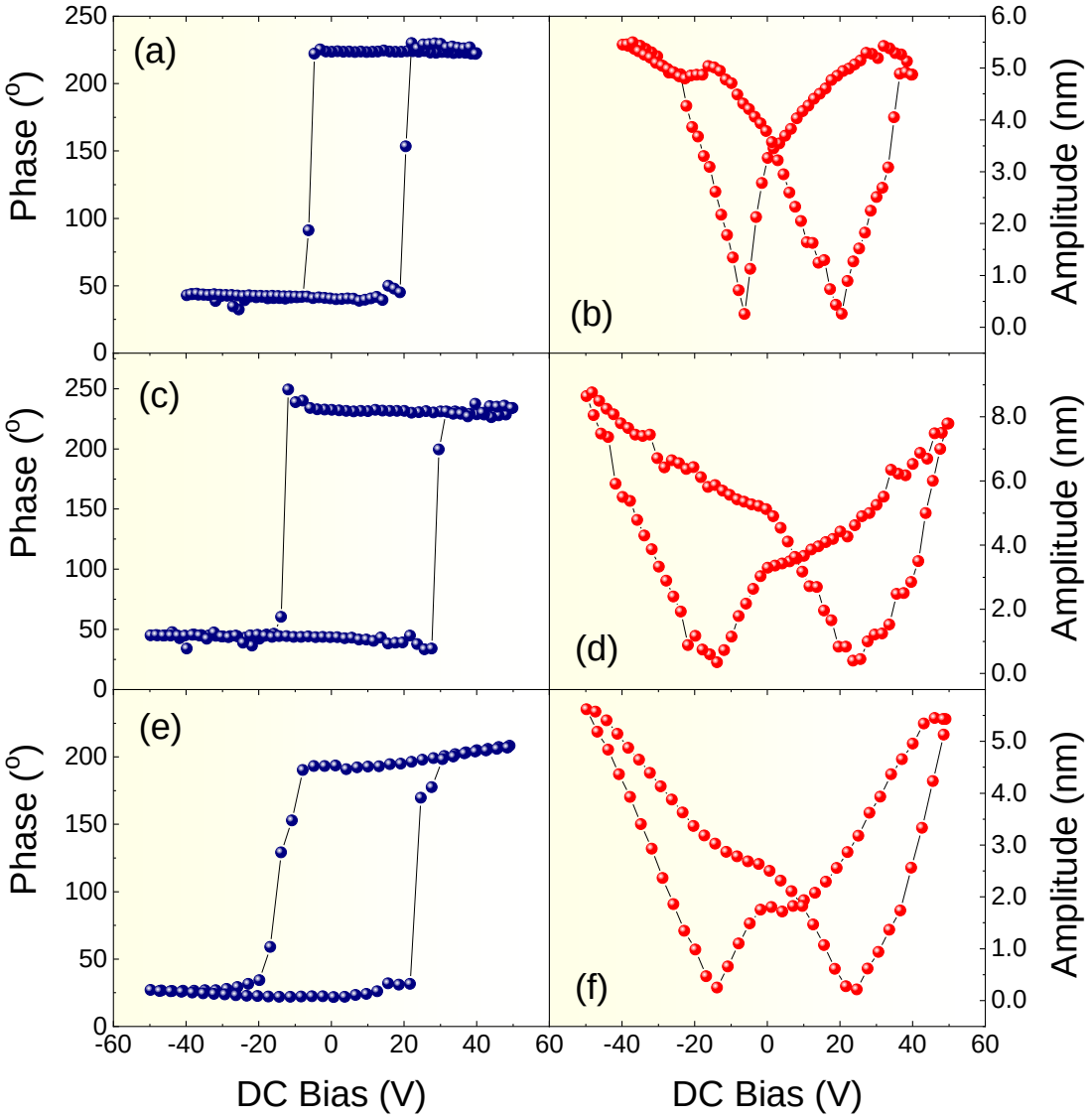

Figure 8. Mendez-González et al.

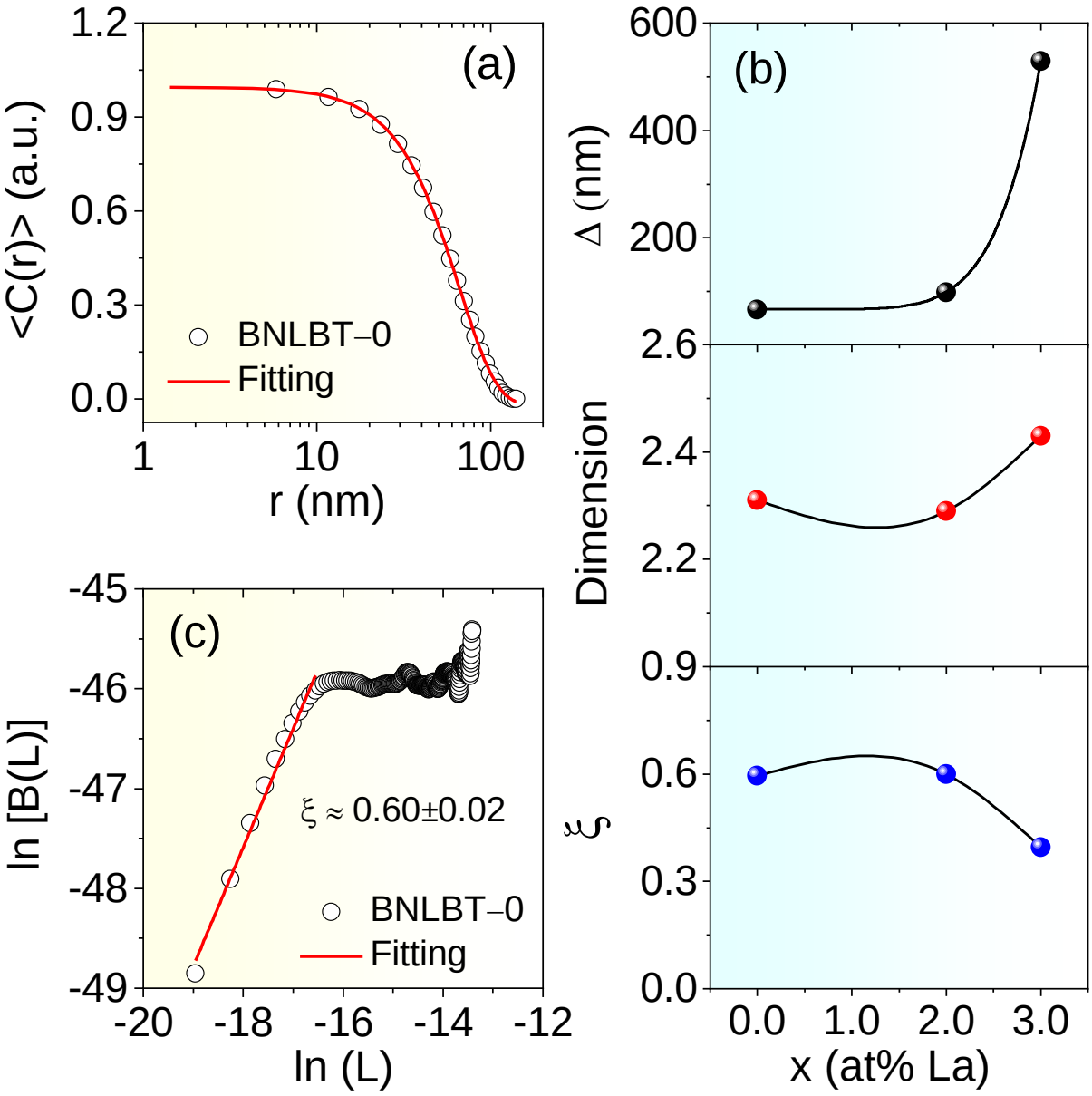

Figure 9. Mendez-González et al.